J Solid State Electrochem (2015) 19:1905–1931
DOI 10.1007/s10008-014-2570-4

REVIEW

Electrochemically assisted deposition by local pH tuning: a versatile tool to generate ordered mesoporous silica thin films and layered double hydroxide materials

Christine Mousty · Alain Walcarius

Received: 13 May 2014 / Revised: 2 July 2014 / Accepted: 3 July 2014 / Published online: 2 August 2014

Abstract This review presents the interest of electrochemistry for the preparation of two families of porous materials (ordered mesoporous silica and layer\ed double hydroxide), generated as thin films on solid electrode surfaces via an electrochemically assisted local pH tuning. The deposition mechanism is dependent on the target material. The driving force to get the ordered mesoporous silica thin films is the combination of electrochemical interfacial surfactant templating to the electro-assisted sol-gel deposition, leading to the growth of vertically aligned mesopore channels of surfactant-templated silica. The mechanism involved in the generation of layered double hydroxide (LDH) thin films is the electrochemically induced precipitation of the material by the electrogenerated hydroxide anions, which can be also applied to the formation of LDH-based composites. After a presentation of the materials that can be synthesized by the electrochemical manipulation of localized pH at electrode/solution interfaces, their characterization and applications are also briefly discussed.

Introduction

The chemical modification of electrode surfaces has generated tremendous research activities, in electrochemistry and beyond, for the last 3 decades [1]. The reason for such marked interest has probably to be found in that chemically modified electrodes combine in a single device the intrinsic properties of selected compounds (called "modifiers") to particular redox processes occurring at electrode/solution interfaces, with dramatic improvement for many electrochemical applications. Among the various electrode modifiers, microporous silicates such as zeolites or clays (or the related layered double hydroxides, LDH), and ordered mesoporous silica-based materials, received great attention from the electrochemist community because they offer attractive properties (e.g., ion exchange capacity, size and/or charge selectivity, hosting capabilities, catalytic or redox activity, and selective recognition or permselective properties), which were largely exploited, notably in electroanalysis [2]. Several reviews have appeared, dealing with electrodes modified with zeolites [3–5], clays [6–9], layered double hydroxides [9–11], and ordered mesoporous solids [12] (including metals [13], carbon [14], or silica-based materials [4, 15, 16]). As many of them are non-electrically conductive, their use in connection to electrochemistry requires a close contact to an electrode surface, which can be basically achieved either by dispersion of powdered materials in bulk composite electrodes or by depositing the material as a thin film onto a solid electrode surface. For this second category (film configuration), as-synthesized materials can be directly casted onto the electrode surface, but this resulted often in poor mechanical stability of the deposits (at the exception of clays and LDHs for which the layered morphology ensured good adhesion to the support). Some other strategies have thus appeared, aiming at the direct preparation of the supported films onto solid electrode surfaces, such as the evaporation-induced self-assembly of ordered mesoporous silica films [17–19] or continuous zeolite films generated by hydrothermal synthesis [20]. More recently, electrochemically assisted deposition methods have been developed, mostly based on pH tuning of the electrode/solution interfacial region, which constitutes the main topic of this review.

C. Mousty
Institut de Chimie de Clermont-Ferrand, ICCF, UMR 6296, CNRS-Université Blaise Pascal, 63171 Aubière Cedex, France

A. Walcarius (✉)
Laboratoire de Chimie Physique et Microbiologie pour l'Environnement, LCPME, UMR 7564, CNRS-Université de Lorraine, 54600 Villers-lès-Nancy, France
e-mail: alain.walcarius@univ-lorraine.fr

Actually, electrodeposition has long been exploited to modify electrode surfaces; many examples are available for metallic coatings, as formed via the reduction of metal ions (Eq. 1) [21, 22], which recently found a resurgence of interest in designing metal nanostructures [23–25], or for polymeric coatings generated by electropolymerization (Eq. 2) [26–28]:

$$M^{n+}_{(aq)} + ne^- \rightarrow M_{(s)} \quad (\mathrm{M} = \mathrm{metal}) \tag{1}$$

$$Monomer_{(aq)} \pm ne^- \rightarrow Polymer_{(s)} \tag{2}$$

Beside such direct electrodeposition, indirect methods have been also developed, mostly based on the electrochemical manipulation of localized pH at the electrode/solution interface. Indeed, the cathodic or anodic electrolysis of water (and/or reduction or oxidation of supporting electrolyte components) is likely to generate, respectively, OH^- or H^+ species on the electrode surface, thus tuning pH in the electrode/solution interface region [29]. This has been notably applied to protonate or deprotonate selected organofunctional groups at chemically modified electrodes in order to improve their electrochemical response [30, 31] or to induce localized solubility changes to deposit functional polymer films (e.g., chitosan [32, 33]). But, probably the main area of application for electrochemically controlled local pH is the synthesis of metal oxides and hydroxides, as well as organoceramics, by cathodic electrodeposition [34, 35]. This is typically achieved from solutions of metal ion precursors, via the indirect precipitation of metal hydroxides (Eq. 3b) by electrogenerated OH^- ions (Eq. 3a), which could be then aged to form oxides, or one-step formation of metal oxides (Eq. 4):

$$2H_2O + 2e^- \rightarrow 2OH^-_{(aq)} + H_{2(g)} \tag{3a}$$

$$M^{n+}_{(aq)} + nOH^-_{(aq)} \rightarrow M(OH)_{n(s)} \left(\rightarrow MO_{n/2(s)} + n/2H_2O\right) \quad (\mathrm{M} = \mathrm{metal}) \tag{3b}$$

$$M^{n+}_{(aq)} + (n-2x)e^- + xH_2O \rightarrow MO_{x(s)} + 2xH^+_{(aq)} \quad (\mathrm{M} = \mathrm{metal}) \tag{4}$$

Actually, besides water reduction (Eq. 3a), there exist various electrolytic reactions that are likely to increase pH at an electrode surface, including reactions that consume protons (e.g., reduction of H^+ or NO_3^-) and reactions that produce hydroxyl species (reduction of H_2O, O_2, H_2O_2, NO_3^-, or ClO_4^-), which can be exploited to prepare ceramic materials [34, 35]. Examples are available for metal oxides such as Al_2O_3 [36], CdO [37], CeO_2 [38], Cr_2O_3 [39], Nb_2O_5 [40], PbO_2 [41], ZnO [42], ZrO_2 [36], and WO_3 [43], among others [34].

A large number of metal hydroxides have been also synthesized by cathodic electrodeposition [34], particularly Ni $(OH)_2$ [44], alone or doped by Co(II) hydroxide [45] for use in alkaline secondary batteries. In 1994, Kamath and colleagues described for the first time the electrodeposition of Ni hydroxides in the presence of trivalent metal cations (Al (III), Cr(III), Fe(III)) [46], leading to the formation of M(II)M (III) hydroxides called layered double hydroxides (LDH).

Ternary oxides and organoceramics [34, 35], as well as calcium phosphate coatings (e.g., hydroxyapatite [47]), can be generated by this way, while codeposition of mixed metal oxides [35, 48] and electrodeposition of inorganic/organic hybrid thin films [49] have been also reported.

Recently, this approach has been successfully combined to nanoscience and nanotechnology to generate metal oxide nanostructures by electrochemically assisted deposition [50–53]. Actually, any kind of material that is likely to be formed upon pH change could be basically generated onto electrode surfaces under electrolytic deposition conditions. Such versatile approach offers advantages such as film formation on substrates of varying geometry and size, patterned or not, simplicity, possibility to tune the film characteristics (composition, structure, thickness, porosity) by controlling the synthesis medium composition and the electrodeposition parameters, and reasonably low cost.

It is therefore not so surprising to have seen the emergence of novel concepts, such as the electrochemically assisted deposition of sol-gel films onto electrode surfaces, as pioneered by Shacham et al. [54]. Here, the electrogenerated OH^- species are not reacting with metal ions in solution, but they contribute to catalyze a sol-gel process [54–57] (i.e., hydrolysis and condensation of metal alkoxide precursors, see Eqs. 5a and 5b in the particular case of silica):

$$Si(OR)_4 + 4H_2O \rightarrow Si(OH)_4 + 4ROH \tag{5a}$$

$$2Si(OH)_{4(aq)} \overset{OH^-}{\rightarrow} (OH)_3Si{-}O{-}Si(OH)_3 + H_2O \tag{5b}$$

The electrodeposition process is characterized by two growing rates: a first slow stage giving rise to rather homogeneous, yet rough, films with thickness in the sub-micrometer range, and a second faster gelification step resulting in much thicker (>1 μm) and rougher

porous deposits [56]. By adding organosilane derivatives in the starting sol, it is possible to prepare organically modified silica films [56, 58] and to induce thereby the emergence of tailored properties such as binding/complexation capacity [59], molecular imprinting [60], superhydrophobicity [61], or protective coatings [62]. Owing to the room temperature sol-gel processing, the method is compatible with the encapsulation of biomolecules, alone [63, 64] or in the presence of gold nanoparticles [65, 66], and even bacteria [67]. It has been also applied to the deposition of composite films (i.e., codeposition of sol-gel/metal [68] and conductive polymer-silica hybrid [69] films) or binary sol-gel films with graded structure [70]. A unique advantage of the electrochemical synthesis of sol-gel thin films, with respect to the classical evaporation approaches, is the possibility to prepare rather uniformly deposited coatings on non-flat surfaces or complex objects, such as printed circuits [71], ordered macroporous electrodes [72, 73], metal nanofibers [74] or carbon nanotubes [75], or stainless steel coronary stent [76]. It also offers the possibility to achieve sol-gel patterning [77, 78] and deposition at the local scale [78, 79]. Applications are expected in the fields of electrochemical sensors [59, 80, 81] and biosensors [75, 81], separation sciences [82], or protection against corrosion [62, 83].

On the other hand, structuration of electrode surfaces at the microporous (<2 nm), mesoporous (2–50 nm), or even macroporous (>50 nm) levels is now becoming an area of intense activity [84–86]. The aim of the present review is thus to highlight the interest of the electrochemical manipulation of localized pH at electrode/solution interfaces to generate such nanostructured thin films, yet with particular emphasis to ordered mesoporous silica-based materials and layered double hydroxides, as both constitute the topic of this special issue and have been developed in our own groups and elsewhere.

Electrogeneration of ordered mesoporous silica films

Ordered mesoporous silica materials constitute a family of uniform pore, silicate-based, mesoporous molecular sieves, discovered almost 20 years ago [87, 88], which were typically obtained by surfactant-assisted synthesis (called liquid crystal templating). The synthetic pathways are usually based on sol-gel processing and involve the controlled assembly of inorganic precursors (such as metal salts or alkoxides, organosilanes, or nanobuilding blocks) around macromolecular or supramolecular templates (such as ionic and non-ionic surfactants, amphiphilic block copolymers, biopolymers, ionic liquids, dendrimers, and polymer colloids). A schematic illustration of the preparation of surfactant-templated hexagonal mesoporous silica (MCM-41) using tetraethoxysilane (TEOS) as the silica source is given in the middle of Fig. 1. Actually, a wide range of porous solids with distinct mesostructures and monodisperse pore sizes (typically tunable from 2 to 30 nm) can be generated by this way [89–91]. They can be also obtained in the form of organic-inorganic hybrids, via either post-synthesis grafting or one-step cocondensation using organosilane reagents [92–94], leading to materials bearing a high number of easily accessible organofunctional groups thanks to the ordered porous mesostructure exhibiting

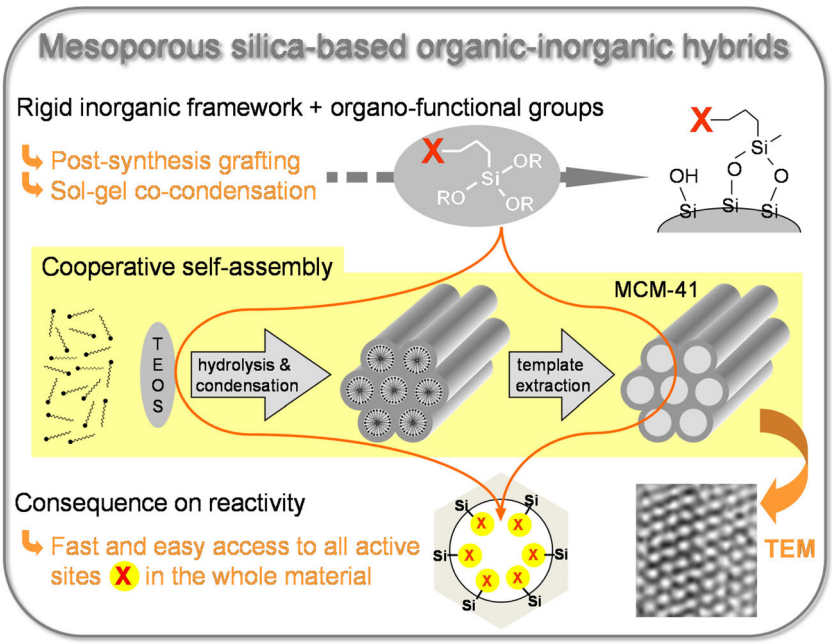

Fig. 1 Illustration of the preparation of mesostructured silica materials by surfactant template-based sol-gel processing and of the strategies applied to get the corresponding organic-inorganic hybrids (a transmission electron micrograph illustrating the hexagonal structure is shown at the *bottom right*)

very large specific surface areas (Fig. 1). They offer promising applications in several fields (electrochemistry, separation, nanomedicine, energy, environment, optics, microfluidics, or sensing), and, if they can be manufactured with various morphologies (powders, monoliths, films, patterns), the design of thin films appears to be very important because this configuration is highly desirable for many practical uses (i.e., in (micro)devices) [95–98]. The most common method to get mesostructured sol-gel thin films is the so-called "evaporation-induced self-assembly" (EISA) process [99–101], which typically involves dip coating from a hydroalcoholic sol and film formation through solvent evaporation (driving self-assembly of silica-surfactant micelles and their further organization into liquid crystalline mesophases, see Fig. 2). As also shown on the figure, a careful control of the starting sol composition and the evaporation conditions enables the formation of various mesostructure types (lamellar, 2D hexagonal, 3D hexagonal, cubic, etc.) [100]. However, getting accessible pores from the film surfaces is essential [95], but it remains challenging to date as most 2D hexagonal structures prepared by EISA are characterized by a horizontal alignment of mesopore channels onto the underlying support, so that efforts to control pore orientation in mesoporous thin films have recently emerged [102, 103], and electrochemistry seems to be an attractive and versatile approach to get mesoporous thin films with pore channels oriented normal to an electrode surface, as discussed below.

Electrochemical interfacial surfactant templating

Adsorption and surface aggregation of ionic surfactants at electrified interfaces can be tuned by varying parameters such as the applied potential, the surfactant concentration, or the hydrophobic/hydrophilic balance of the solid/liquid interface, leading to various surfactant configurations including bilayers, adsorbed spherical or cylindrical micelles, and hemimicelles [104]. Micelles can form at the interface even when the surfactant concentration is lower than the critical micellar concentration. Such electrochemically controlled (i.e., potential-dependent) surfactant organization can be combined to the electrochemical deposition of nanostructured metal or metal oxides, as pioneered by Choi et al. in the Stucky group [105, 106]. This is conceptually distinct from the electrodeposition of mesoporous films (i.e., metallic) from dense surfactant phases formed by soft self-assembly onto electrode surfaces (i.e., lyotropic liquid crystalline phases obtained from concentrated surfactants or block copolymers),

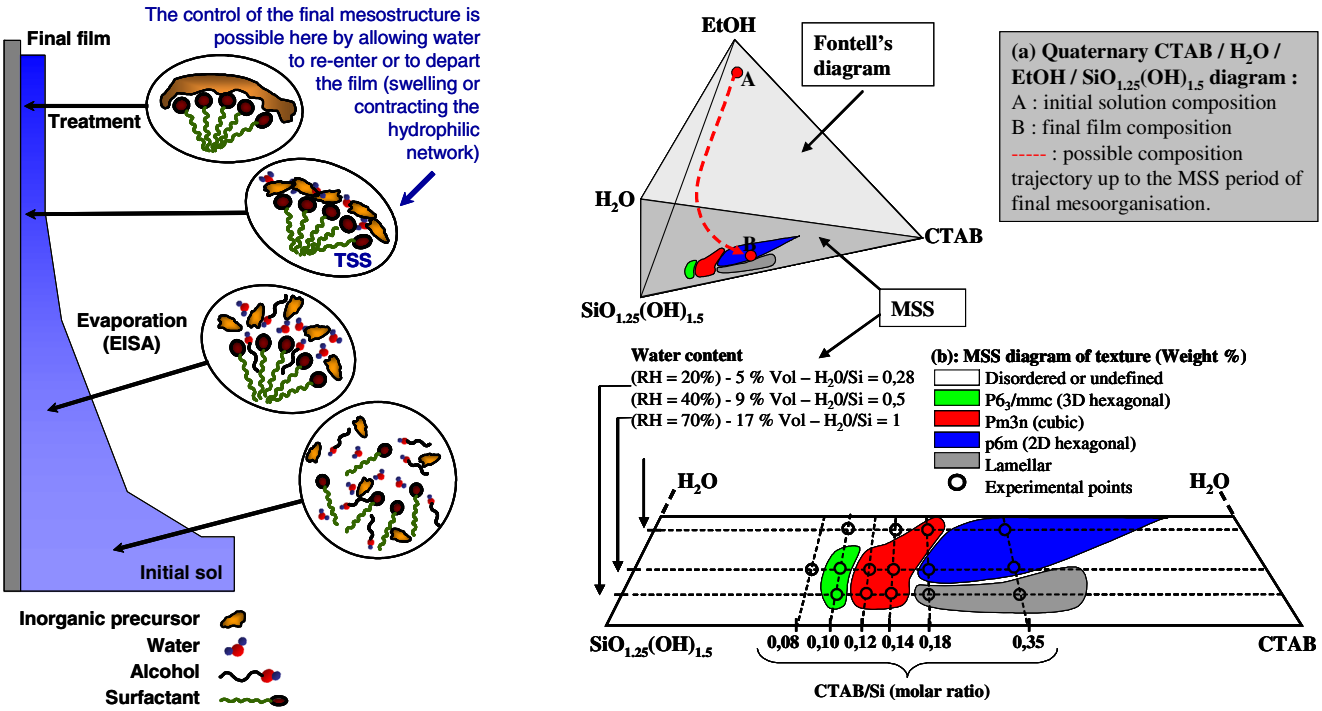

Fig. 2 General scheme illustrating the formation of mesoporous silica thin films by dip coating using the evaporation-induced self-assembly approach (EISA, *left*). Step 1: the isotropic initial sol where the condensation is optimally slowed down. Step 2: the evaporation proceeds and micelles start to form above the CMC. Step 3: the evaporation is complete; the film equilibrates with its environment, and the final mesostructure is selected by adjusting the relative humidity (RH) before further inorganic condensation. Step 4: the inorganic network is condensed; the hybrid microstructure is stabilized. the EISA-adapted diagram of textures established for the $CTAB/SiO_{1.25}(OH)_{1.5}/EtOH/H_2O$ system (in percentage, *right*). The quantity of water in vol%, the molar ratios, and the quantity of CTAB (molar ratio) are also reported. Reprinted with permission from Grosso et al. [100]. Copyright 2004 WILEY-VCH Verlag GmbH & Co. KGaA

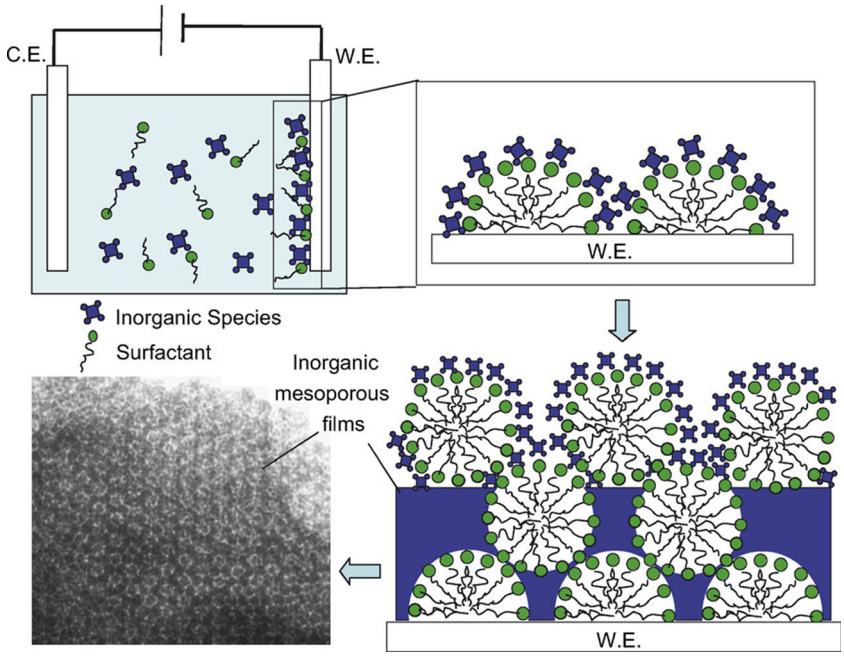

Fig. 3 Schematic representation of an electrochemical interfacial surfactant templating method. An interfacial amphiphilic assembly composed of hexagonally close-packed spherical micelles is used as a template in this scheme. Reprinted with permission from Tan et al. [118]. Copyright 2005 American Chemical Society

acting as a casting template, the ordered mesoporous metals being formed by reduction of metal salts confined to the aqueous environment of these phases [107–109]. The principle of the electrochemical interfacial surfactant templating method (Fig. 3) involves the concomitant assembly of amphiphilic molecules under potential control and the electrochemical deposition of the inorganic phase in a self-assembly growth process [110]. A prerequisite is to ensure strong interaction between the inorganic precursors (e.g., metal ions) and the hydrophilic heads of the amphiphiles, in order to enable continuous construction of interfacial inorganic-organic assemblies (Fig. 3). The first examples were semiconducting and metallic nanostructured films (i.e., ZnO [103] or platinum [106]) generated by either electroreduction of metal ions (Eq. 1) or electrochemically induced precipitation of metal (hydr)oxides (Eqs. 3 and 4) in the presence of ionic surfactants as sodium dodecyl sulfate (SDS) or cetyltrimethylammonium bromide (CTAB). Then, the method was extended to the generation of other mesostructured metal oxides or hydroxides, such as mesoporous $Ni(OH)_2$ [111], $Co(OH)_2$ [112], WO_3 [113], birnessite-type manganese oxides [114], Co_3O_4 [115], SnO_2 [116], MnO_2 [117], and always much activities on mesoporous ZnO [118–123]. Zinc and manganese oxide films with ordered lamellar structures were also obtained by anodic deposition in basic media using the interfacial surfactant templating method [117, 119]. Lamellar mesostructures were most often observed [124] (see an illustration for ZnO in Fig. 4), but 2D hexagonal and 3D wormlike structures have been also reported [110], and recent efforts have been made to better control the orientation, the anisotropy, or the morphology of electrodeposited mesoporous ZnO films [120, 121, 123].

The electroassisted self-assembly method to prepare mesoporous silica films

The above electrochemical interfacial surfactant templating method was thus first applied to the direct electrodeposition of mesoporous metals and metal oxides, but taking into account that sol-gel films can be also generated onto electrode surfaces by electrochemically assisted deposition [54–57], one should be able to deposit sol-gel-derived mesoporous silica films by this way. This concept was first developed by Walcarius et al. [125]. It involves the application of a suitable cathodic potential (approximately −1.3 V) to an electrode immersed in a hydrolyzed sol solution (e.g., TEOS-based) containing a surfactant template (i.e., CTAB) to generate the hydroxide ions that are necessary to catalyze polycondensation of the precursors in the form of a silica thin film (see top of Fig. 5), concomitantly to the formation of a transient surfactant hemimicelle inducing the growth of hexagonally packed one-dimensional channels of about 2 nm in diameter perpendicularly to the electrode surface (see bottom of Fig. 5). In the presence of surfactant, the polycondensation of silica precursors is much faster than without CTAB (i.e., the case discussed in the third part of the "Introduction" section). Contrary to the aforementioned mesoporous metals and metal oxide, the electrochemical deposition is indirect in the sense that the generated OH^- species act as a catalyst enabling the film formation. Actually, the applied potential plays two roles: the generation of OH^- catalyst and the controlled surfactant

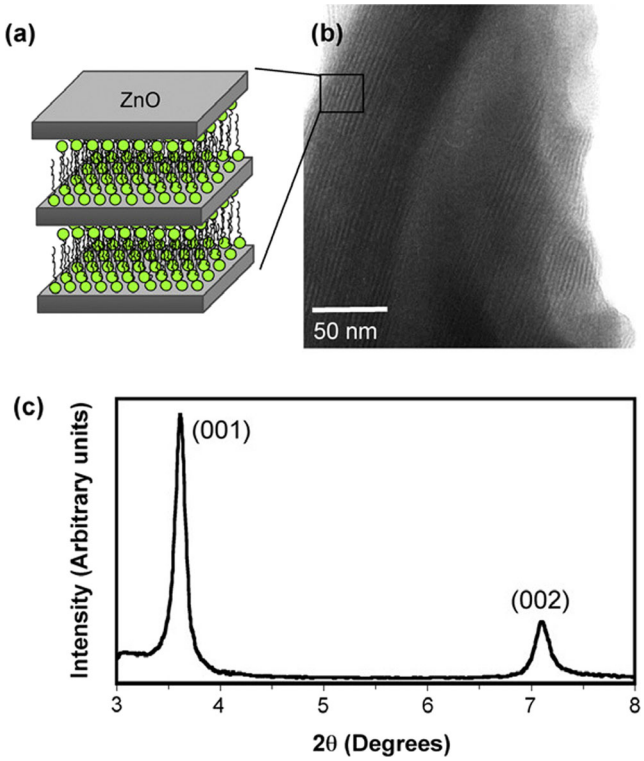

Fig. 4 **a** Lamellar structured ZnO films templated by bilayer assembly of surfactants. Typical **b** TEM and **c** small-angle XRD pattern of lamellar structured films are also shown. These films were deposited from 0.02-M zinc nitrate solutions containing 0.25 wt% of AOT as the structure directing agent (d_{001}=2.6 nm). Reprinted in part with permission from Tan et al. [118]. Copyright 2005 American Chemical Society

self-assembly onto the electrode surface. Such films can be obtained, either potentiostatically or galvanostatically [126], on various conducting substrates, such as metallic (Au, Pt, Cu) or carbon electrodes [125, 126], indium-tin oxide (ITO) [126], or silicon wafer [127]. They can even be prepared on non-conductive surfaces (such as polystyrene), but this requires the use of feeder electrodes (i.e., two carbon plates sandwiching the polystyrene substrate) and larger applied potentials (i.e., 3.6 V); in that case, the driving force for film formation is the pH gradient induced by the high electric field and not any polarization of the support because of its insulating properties [128]. The thin films are uniformly deposited onto the underlying support (Fig. 6a), and their thickness can be tuned typically in the 25–150-nm range by adjusting either the TEOS concentration or the electrosynthesis parameters (applied potential of current densities, deposition time) [126]. However, as a result of the generated OH^- species in a diffusion layer of hundreds of microns in thickness at the electrode/solution interface, an unwanted side product made of aggregates (approximately some micrometers in thickness) can be formed over the thin film (Fig. 6b), especially at long deposition times or highly cathodic potentials [125]. The particles constituting these aggregates are also surfactant-templated, but their mesostructure is wormlike and not as well defined as the underlying thin film. High-resolution transmission electron microscopy (TEM) examination of the thin film reveals indeed the presence of highly ordered, hexagonally packed mesopore channels (as also confirmed by the electron diffraction pattern, see Fig. 6c), with perfect orthogonal orientation with respect to the film plane (Fig. 6d). It was shown that the highly ordered and oriented mesoporous silica films can be obtained over a wide composition of the starting sol (i.e., 10–200 mM CTAB and 50–350 mM TEOS), with film thickness that can be tuned typically between 50 and 150 nm, and that the lattice parameter can be moderately tuned by changing the chain length of the surfactant template [126]. An important parameter ensuring the good level of ordering and mesopore orientation is the CTAB/TEOS molar ratio that should be kept in the 0.16 to 0.64 range. Such vertical alignment of mesopore channels is highly desirable for practical applications as it ensures fast mass transport to external reagents, but it remains challenging to date. Electrochemistry thus offers a versatile way, yet simple, to get such oriented mesoporous films. Alternative strategies to generate vertically aligned mesoporous silica films include the following [103]: the dimensional confinement and self-assembly process in exotemplates (preassembled block copolymer films [129–131] or porous membranes [132, 133]), the resort to patterned supports or combination of photoaligning and micropatterning techniques or surface-mediated alignment via π-π interactions [134], the epitaxial growth [135], the magnetically induced orientation [136], or a Stöber-solution growth method [137].

Beside simplicity and robustness, another unique advantage of the electroassisted self-assembly (EASA) method is its suitability to generate mesoporous silica films on non-flat surfaces [125]. This is illustrated on Fig. 7 for the particular case of a so-called gold CD-trode (i.e., a gold electrode made from recordable CD) [138]. The interest of such support is its regular streaked morphology made of arrays of mounds and trenches of 100 nm in height (Fig. 7a), which corresponds to the order of magnitude of the EASA-deposited mesoporous thin films (i.e., 80 nm in the present case, see Fig. 7b), and for which both atomic force and electron microscopy characterizations clearly indicate the advantage of EASA over EISA in getting mesostructured deposits of uniform thickness (Fig. 7c–g). Electrochemically assisted deposition was also successfully applied to the growth of mesoporous silica films on carbon fibers (7–8 μm in diameter) and platinum ultramicrodiscs (25–50 μm in diameter) [139], which are very difficult to obtain using other existing methods. Finally, the EASA approach is also suitable for the generation of patterned deposits of mesostructured materials, as demonstrated for the selective generation of mesostructured silica films on copper arrays of variable width (100–500 μm) on a polymer substrate, without any deposition on the polymer part of the substrate [125].

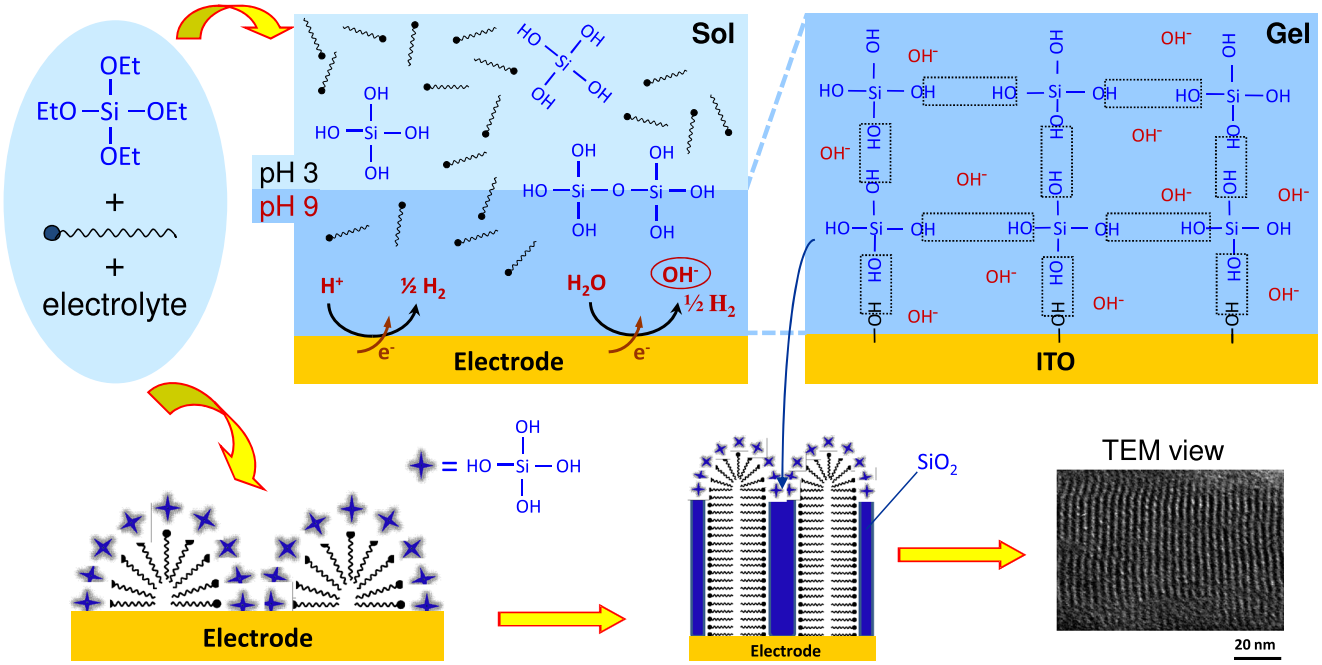

Fig. 5 Schematic representation of the EASA process starting from a sol solution containing a silica precursor (TEOS), a surfactant (CTAB), and an electrolyte at pH 3. The *top* of the scheme illustrates the electrochemically induced polycondensation upon pH increase at the electrode/solution interface, while the *bottom part* shows the electrochemical interfacial surfactant templating of a vertically aligned mesoporous silica film (along with TEM view)

The EASA method can be combined to colloidal crystal templating [140], in order to get thin silica films with hierarchical porosity (i.e., bimodal and macroporous-mesoporous) [141]. To this end, the electroassisted deposition of mesoporous silica material is performed inside a polystyrene bead assembly, by filling of voids between the polystyrene bead template, resulting in a bimodal macro-meso structure after removal of the beads (Fig. 8a). Interestingly, the preferential mesopore orientation is maintained over the entire film thickness, through the whole space defined by the polystyrene bead assembly (Fig. 8b). Thanks to the combination of interconnected macropores and mesopores, fast mass transport is ensured, faster than the corresponding monomodal macrostructured or mesostructured films [141]. On the other

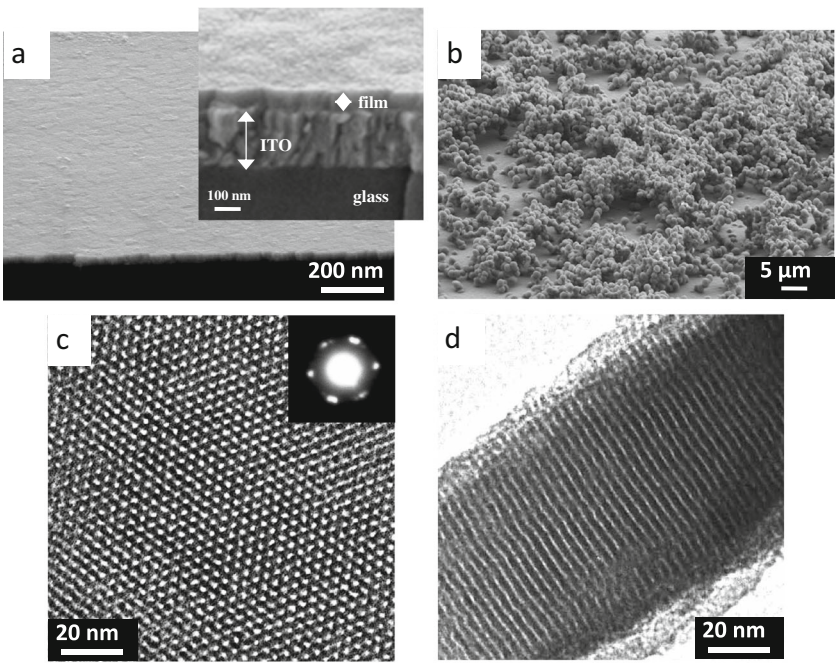

Fig. 6 **a**, **b** FE-SEM micrographs obtained for electrodeposited surfactant-templated mesoporous silica films on ITO, as generated at two distinct electrodeposition times: 10 s (**a**) and 30 s (**b**); the inset in part of Fig. 6a is an enlargement of the cross-sectional view obtained after vertical cleaving of the sample. **c**, **d** TEM micrographs obtained for a surfactant-templated mesoporous silica film electrogenerated on glassy carbon: high-magnification top view (**c**), high-magnification cross-sectional view (**d**); the inset of Fig. 6c shows the electron diffraction pattern of the mesostructured film. Reprinted in part with permission from Walcarius et al. 125]. Copyright 2007 Nature Publishing Group

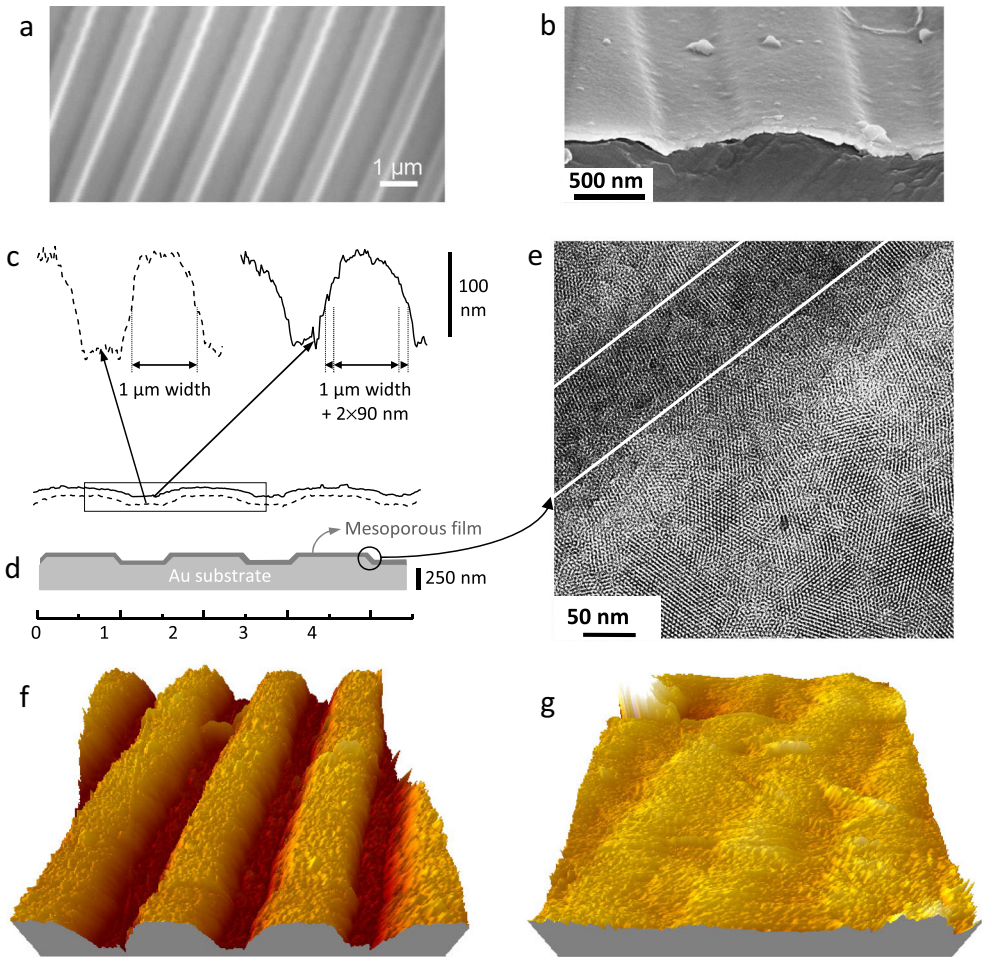

Fig. 7 **a**, **b** Microscopic characterization of a film electrodeposited on a gold CD-trode (gold electrode made from recordable CD, displaying a regular streaked morphology at the micrometer size level): SEM micrographs obtained before (**a**) and after (**b**) film deposition. **c** AFM height profiles measured perpendicularly to the streaked gold substrate before (*dashed line*) and after (*plain line*) deposition of the mesoporous silica film, showing clearly the uniform thickness (~90 nm) of the thin film deposited on the whole surface of the regular streaked support. *Dotted lines* indicate the thickness of the film deposited on the vertical parts of the substrate. **d** Scheme of the underlying substrate. **e** TEM micrograph of the film showing that mesostructuration is retained on non-planar portions of the surface (between the *white lines*). **f**, **g** 3D AFM images (size 5 by 5 µm, *x*/*y*/*z* ratios taken as 1/1/5) of the film prepared by EASA on the gold CD-trode (Fig. 7f is the same sample as Fig. 7b) and of a film prepared by spin coating evaporation-induced self-assembly (**g**); this points out the limitation of the spin coating process to deposit uniform films on non-flat surfaces as the streaked profile of the underlying gold substrate is not maintained after film deposition. Reprinted in part with permission from Walcarius et al. [125]. Copyright 2007 Nature Publishing Group

hand, using a scanning electrochemical microscope (SECM) enables one to deposit microdots of surfactant-templated silica [142]. It can be used in either the tip generation mode (i.e., using the SECM tip as working electrode, see Fig. 9a) or in an indirect mode (i.e., using the SECM tip as counter-electrode, see Fig. 9b). In both cases, the OH^- catalyst is generated in a spherical domain in the tip-substrate region (Fig. 9a, d). In the former case, well-define microdots can be obtained (Fig. 9b) on both conductive or insulating substrates, but the resulting material is poorly ordered in the form of wormlike structure (Fig. 9c). On the other hand, using the indirect mode led to a good level of ordering with hexagonally packed mesopore channels oriented normal to the underlying support (Fig. 9f), but deposition was evidently only possible on conductive substrates. It should be kept in mind that observation of the films by transmission electron microscopy (TEM) was only possible after collecting portions of the material onto TEM grids. The direct observation of the regular patterning was, however, possible using microscopy and X-ray photoelectron spectroscopy (XPS) analysis imaging (Fig. 9e), demonstrating the successful local deposition only in the SECM tip region. This tip can thus be used as a micrometric "pen" inducing self-assembly polycondensation of the precursors by local pH change under potential control, opening the door to sol-gel electrochemical lithography. Moreover, the fact that the oriented mesostructure was only observed when biasing the underlying support at a cathodic potential contributes to

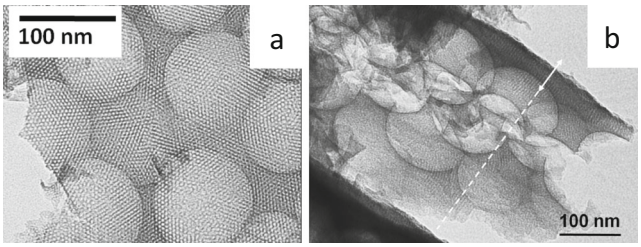

Fig. 8 TEM micrographs (**a** top view and **b** cross section) of bimodal mesoporous silica films prepared by electrochemically assisted sol-gel deposition from a TEOS/CTAB medium inside a polystyrene bead assembly. Reprinted with permission from Etienne et al. [141]. Copyright 2010 American Chemical Society

support the electrochemical interfacial surfactant templating mechanism discussed above.

All the above examples of mesoporous silica films obtained by EASA were based on hydroalcoholic sols, and, when mesostructuration was effective, this was always in the form of hexagonally packed and vertically aligned mesochannels. Very recently, attempts were made to prepare surfactant-templated silica films by EASA from water-based sols (i.e., without added a cosolvent) [142]. A fundamental change when passing from a 50:50 water/ethanol mixture to pure water is the dramatic drop in the critical micellar concentration (CMC) of CTAB from 22 to 0.9 mM [143]. In such case, it was mandatory to "play" with the chaotropic-cosmotropic character of the surfactant counter-anions to control the morphology and surfactant assembly changes arising from such lower CMC values. Chaotropic agents (i.e., disorder-maker) are expected to destabilize hydrophobic aggregates while cosmotropic ones (i.e., order-maker) play a stabilizing role. On the basis of the Hofmeister series [144], it was observed that cosmotropic anions (such as SO_4^{2-}) promote the formation of thin films but suffering from poor or no ordering, whereas weakly bonded anions (such as Cl^-) favor the mesostructuration but mainly in the form of particles or aggregates, while chaotropic anions (such as Br^-) lead to rather thick deposits made of poorly organized aggregates [142]. Mixing these anions, to get mixed micelles, enables to reach compromises between these "extreme" behaviors, and mesostructured thin films can be indeed obtained with the $CTACl/Na_2SO_4$ and $CTABr/Na_2SO_4$ media, exhibiting respectively some vertical or horizontal orientation of mesopore channels. An illustration of the horizontal orientation can be seen on the right part of Fig. 10.

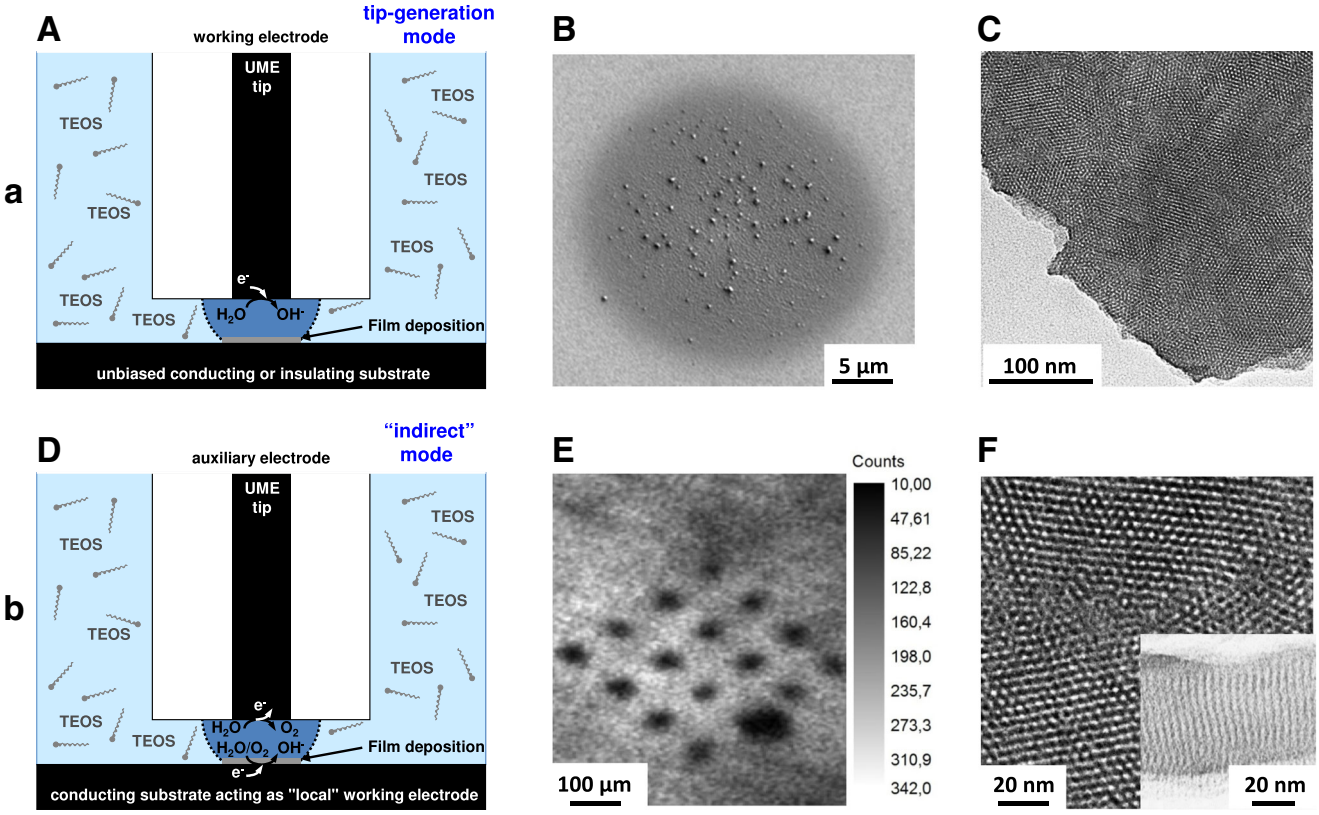

Fig. 9 Local deposition of surfactant template mesoporous silica dots by SECM, achieved either in the tip generation mode (**a**) or in an indirect mode (**b**). **A**, **D** expanded view of the UME−substrate region for both tip generation mode (**A**) and indirect mode (**D**), including redox reactions involved in the processes. **B** SEM and **C** TEM micrographs of a dot electrodeposited on ITO using the tip generation mode. **e** XPS imaging at the In_{3d} line (444.7 eV) of 16 microdots prepared by the indirect mode and **f** the corresponding TEM micrographs (top and cross-section views). Samples were prepared using a 25-µm-diameter Pt UME (SECM tip) immersed in a 340-mM TEOS solution containing a CTAB content adjusted to reach $[n_{CTAB}/(n_{TEOS})]=0.32$. Reprinted with permission from Guillemin et al. [142]. Copyright 2011 American Chemical Society

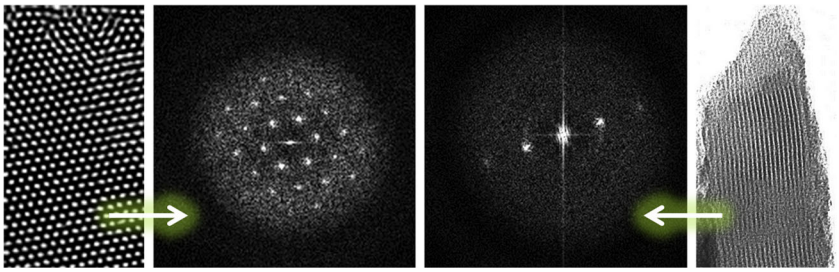

Fig. 10 TEM micrographs (*external*) and electron diffraction patterns (*center*) of mesoporous silica films prepared by electrochemically assisted sol-gel deposition from a 50:50 water/ethanol TEOS/CTAB/$NaNO_3$-based sol (*left*) and from an aqueous TEOS/CTAB/Na_2SO_4-based sol (*right*). Reprinted with permission from Guillemin et al. [142]. Copyright 2014 American Chemical Society

Finally, though not being ordered at the mesoscale, other kinds of template silica films formed by electrochemically initiated sol-gel processing have been reported, using generation 4 poly(amidoamine) (PAMAM) dendrimer to facilitate pore formation [145]. Such films exhibiting pore size of ~10 nm offered size-exclusion properties, and using poly(styrene sulfonate) nanobeads instead of PAMAM resulted in increasing pore size of up to 50 nm [146].

Characterization of the oriented mesoporous silica films

In addition to the direct microscopic observations (Figs. 6–9), diffraction techniques can be used to evidence the mesostructural order and/or the pore orientation. Combined to TEM analysis, electron diffraction provides information on the mesostructure type. It can for instance distinguish between the typical vertically aligned hexagonal mesostructure obtained by EASA in hydroalcoholic medium and the horizontally oriented films prepared from aqueous sol solutions (Fig. 10). However, the most appropriate diffraction techniques to evidence the vertically aligned mesopore channels are those operating at grazing incidence, such as grazing incidence X-ray diffraction (GIXD, e.g., Goux et al. [126]) or grazing incidence small-angle X-ray scattering (GISAXS, e.g., Cheng et al. [127]). As illustrated in Fig. 11, both GISAXS (Fig. 11a–d) and GIXD (Fig. 11e, f) are likely to evidence the vertical mesopore orientation via the typical diffraction spots in the equatorial plane of the GISAXS and GIXD patterns. They indicate a high level of mesostructural order in the silica film and perfect alignment of mesochannels normal to the underlying support over square centimeters area. The diffraction spots can be ascribed to the (10), (11), (20), and (21) planes of the hexagonal p6m pore arrays, with lattice parameters that can be slightly adjusted in the 3–3.5-nm range

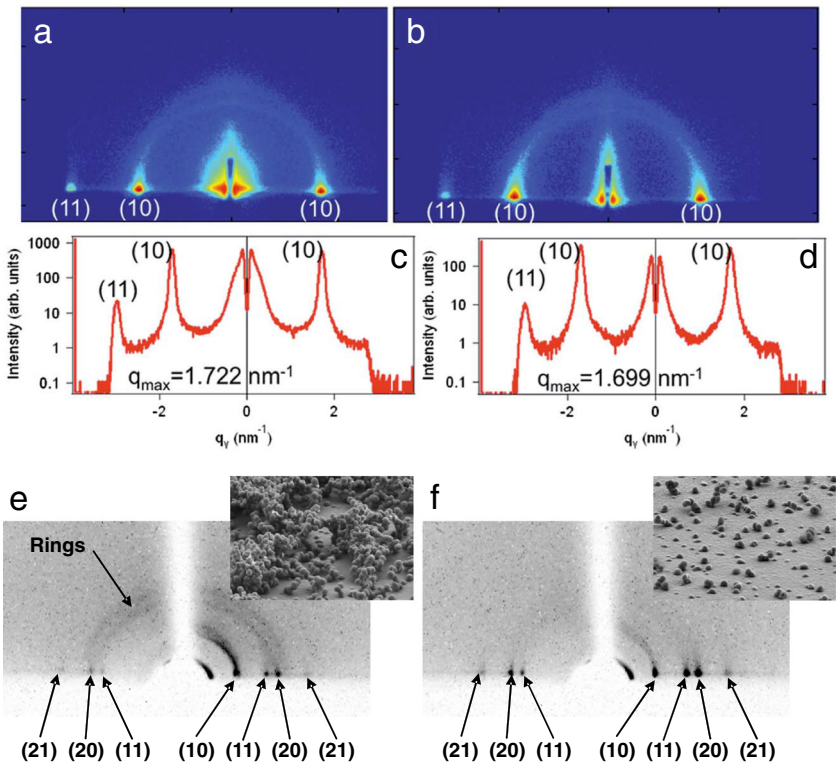

Fig. 11 **a**–**d** 2D GISAXS patterns of mesoporous silica films electrogenerated on two substrates: PEDOT:PSS-coated ITO (P-ITO) (**a**) and a doped silicon wafer (**b**); 1D GISAXS pattern of the mesoporous films on **c** P-ITO and **d** silicon wafer (PEDOT:PSS is poly (3,4-ethylenedioxythiophene): poly(styrenesulfonate)). Reprinted with permission from Cheng et al. [127]. Copyright 2014 Royal Society of Chemistry. **d**–**f** GIXD patterns of EASA-produced mesoporous silica films before (**e**) and after (**f**) removal of most particulate aggregates. Reprinted with permission from Goux et al. [126]. Copyright 2009 American Chemical Society

by varying the alkyl chain length of the ammonium surfactant (corresponding to pore sizes tuneable in the 1.3–3.3-nm range) [147]. The lattice parameters remain unchanged after surfactant extraction. Also, the appearance of out-of-plane rings enables us to evidence the wormlike mesostructure of the aforementioned aggregates, when present in addition to the oriented thin film (Fig. 11e). GISAXS and GIXD characterization is important as it offers a unique way to get information on the film structure in a non-destructive way (contrary to TEM observation, which requires scratching of a film portion prior to analysis). Note that classical Bragg-Brentano X-ray diffraction (XRD) is not likely to evidence such vertical mesostructures [126].

A detailed structural investigation of oriented mesoporous silica films generated by EASA has been provided by Xu et al. [148]. On the basis of careful TEM examination, they confirm the initial observation [125] of nanosized domains which exhibit hexagonal patterned channels uniquely projecting normal to the film surface but rotate by a certain angle with respect to each other. Grain boundaries either parallel or normal to the channel direction have been evidenced (see some examples of lattice displacement in Fig. 12a–e), and such boundary regions showed various structural features such as lattice distortion, lattice displacement, dislocation, coincidence site lattices (small-angle tilt boundary and triple junction can be seen on Fig. 12f–g). Such microstructure variations are expected to affect the properties and subsequent applications of the film.

Several electrochemical techniques, such as cyclic voltammetry (CV), hydrodynamic (volt)amperometry (i.e., linear voltammetry at rotating disc electrode (RDE) or amperometry with a wall-jet cell (WJC)), and scanning electrochemical microscopy (SECM), can be used to characterize the permeability properties of mesoporous silica thin films. As details on these qualitative and quantitative approaches have been previously reported [147], only a brief summary, along with some typical illustrations, is given hereafter. CV provides a fast and effective mean to check the full coverage of the underlying support with the mesoporous film, via the absence of any signal for hydrophilic redox probes (such as $Ru(NH_3)_6^{3+}$, $Ru(bpy)_3^{2+}$, I^- or $Fe(CN)_6^{3-}$) prior to surfactant extraction owing to the impossibility for the probe to reach the electrode surface in the absence of significant defects or cracks (Fig. 13a, dotted line). After template removal, well-defined peaks are now obtained (Fig. 13a, dashed line), even larger than for the same $Ru(NH_3)_6^{3+}$ probe at the bare electrode (Fig. 13a, plain line),

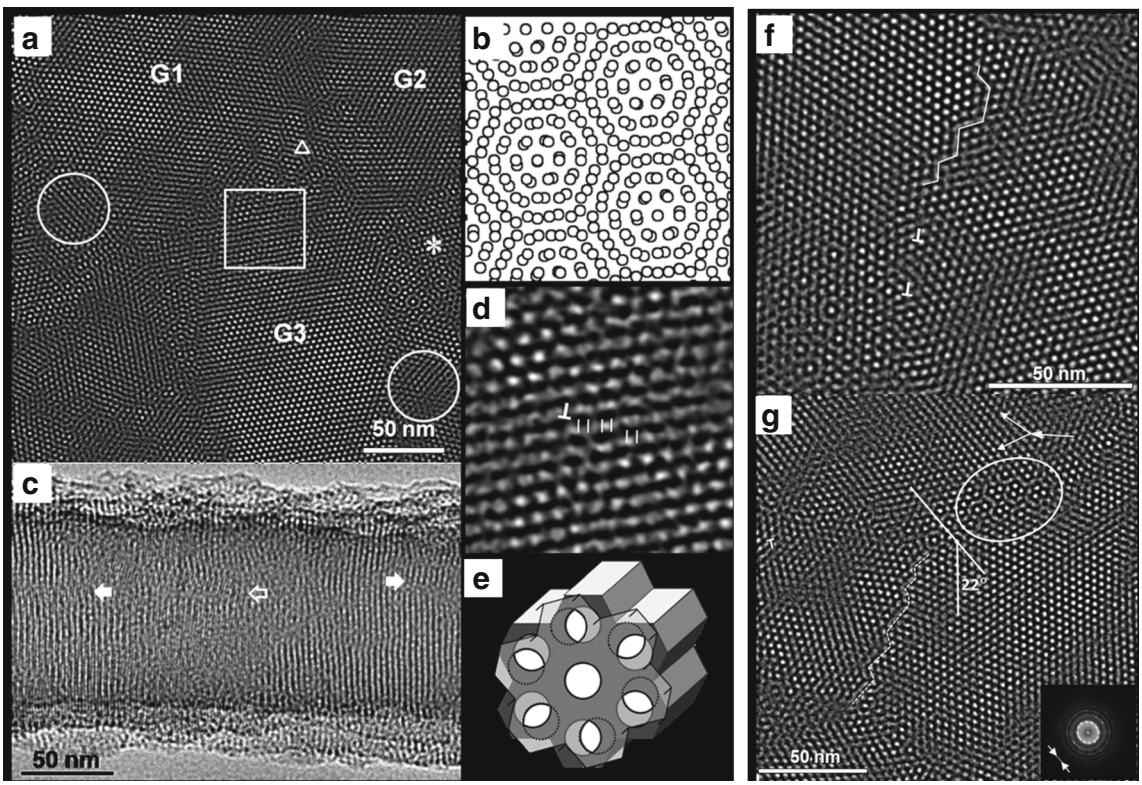

Fig. 12 **a** TEM plan view of an oriented mesoporous silica film generated by EASA illustrating the presence of three distinct "grains" (G1–G3), different structural features (including Moiré fringes, Δ). **b** Structural model of a Moiré pattern. **c** TEM cross-section image of the film (structural defects at *arrows*). **d** Enlarged image of the area framed by a *square* in Fig. 12a showing lattice displacement. **e** Schematic drawing of the channel configuration at the superimposed region. **f**, **g** TEM micrographs of grain boundaries: small-angle tilt boundary (F) and a triple junction (G) where the *arrows* refer to the displacement vectors (the *inset* shows the diffractogram of the area in Fig. 12g, in which *arrows* represent the internal stresses). Reprinted with permission from Xu et al. [148]. Copyright 2010 American Chemical Society

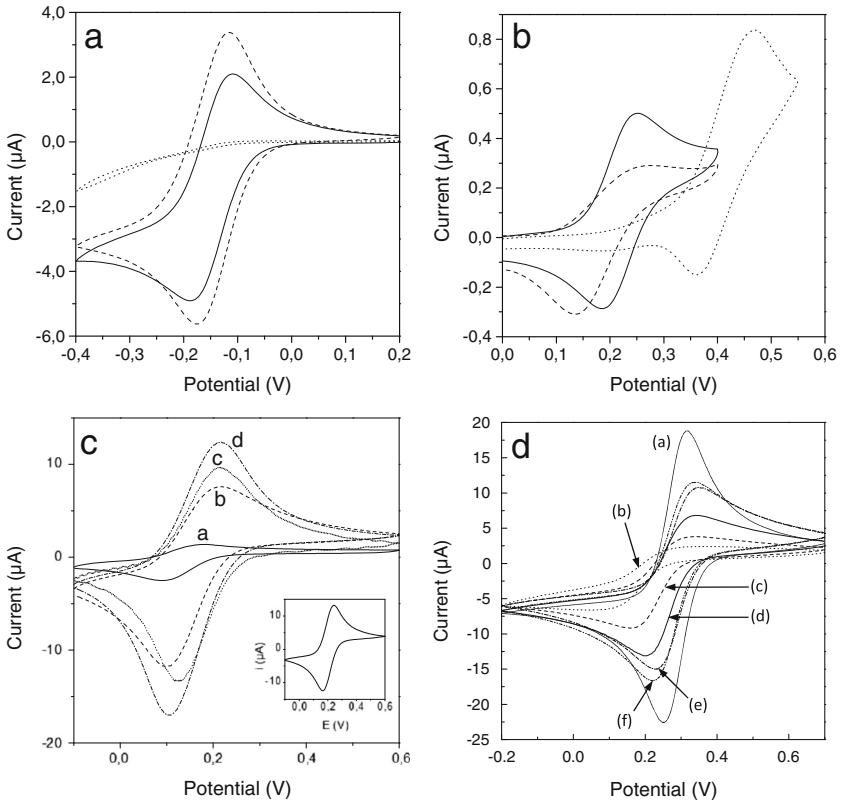

Fig. 13 Electrochemical monitoring of the permeability properties of mesoporous silica films generated by EASA. **a**, **b** Cyclic voltammograms recorded in 5 mM $Ru(NH_3)_6^{3+}$ (**a**) or 0.5 mM ferrocene ethanol (**b**) using a bare gold substrate (*solid lines*) and the same electrode covered with the mesoporous film before (*dotted lines*) and after (*dashed lines*) surfactant removal. Reprinted with permission from Walcarius et al. [125]. Copyright 2007 Nature Publishing Group. **c** Cyclic voltammograms recorded in 0.5 mM ferrocene ethanol at ITO electrodes covered by mesoporous silica thin films generated using various surfactants: C_{12}TAB (*a*), C_{14}TAB (*b*), C_{16}TAB (*c*), and C_{18}TAB (*d*) (curves obtained after surfactant extraction). The response of the bare electrode is given in *inset*. The surfactant/TEOS molar ratio was adjusted depending on the surfactant. It was 0.5 for C_{12}TAB and C_{14}TAB, and 0.32 for C_{16}TAB and C_{18}TAB. Reprinted with permission from Goux et al. [126]. Copyright 2009 American Chemical Society. **d** Cyclic voltammograms recorded in 0.5 mM $K_3Fe(CN)_6$ using a bare ITO electrode (*a*) or ITO covered with a mesoporous silica thin film after template extraction (*b*–*f*), as recorded in the presence of increasing KCl concentrations: 0.1 M (*b*), 1 M (*c*), 2 M (*d*), 3 M (*e*), and 4 M (*f*). Reprinted with permission from Goux et al. [150]. Copyright 2009 Springer

indicating fast diffusion through the film (and some accumulation of the positively charged probe by electrostatic binding to the negatively charged silica surface). Such behavior was already reported for other mesoporous silica films (i.e., formed by evaporation) [18, 149], but the observed currents after template extraction were significantly lower than here, confirming the interest of the vertical orientation of mesopore channels to ensure fast mass transport processes. The voltammetric signature was different when using the neutral ferrocene ethanol probe (Fig. 13b), giving rise to a well-defined signal prior to template removal but shifted toward the anodic side (due to solubilization, and thus stabilization, of the probe into the liquid-crystal-like surfactant phase), and then a typical solution-phase response after surfactant extraction, yet slightly lower than that recorded on the bare electrode due to some resistance to mass transport through the 2-nm-diameter pores. Some modulation of the film permeability can be achieved by varying the pore diameter (i.e., using surfactants with distinct size in the alkyltrimethylammonium bromide family, C_xTAB[126]), as illustrated in Fig. 13c, showing also that a loss in the mesostructure and/or pore orientation (i.e., the case of C_{12}TAB) resulted in a dramatic drop in the film permeability properties. Using a negatively charged probe (e.g., $Fe(CN)_6^{3-}$) led to a rather poor permeability of the film due to strong electrostatic repulsion from the negatively charged silica surface, but this effect can be somewhat reduced by increasing the electrolyte concentration (Fig. 13d) [150], thanks to Donnan effects, as also shown for other porous silica films [145].

A more quantitative approach to permeability characterization is the work under hydrodynamic conditions. Using either RDE [151] or WJC [152], it is possible to evaluate the apparent diffusion coefficients of selected redox probes (e.g., ferrocene ethanol derivatives) in such mesoporous thin films, as illustrated in Fig. 14 for the particular case of silica films bearing increasing amounts of methyl groups (see the "Strategies to get

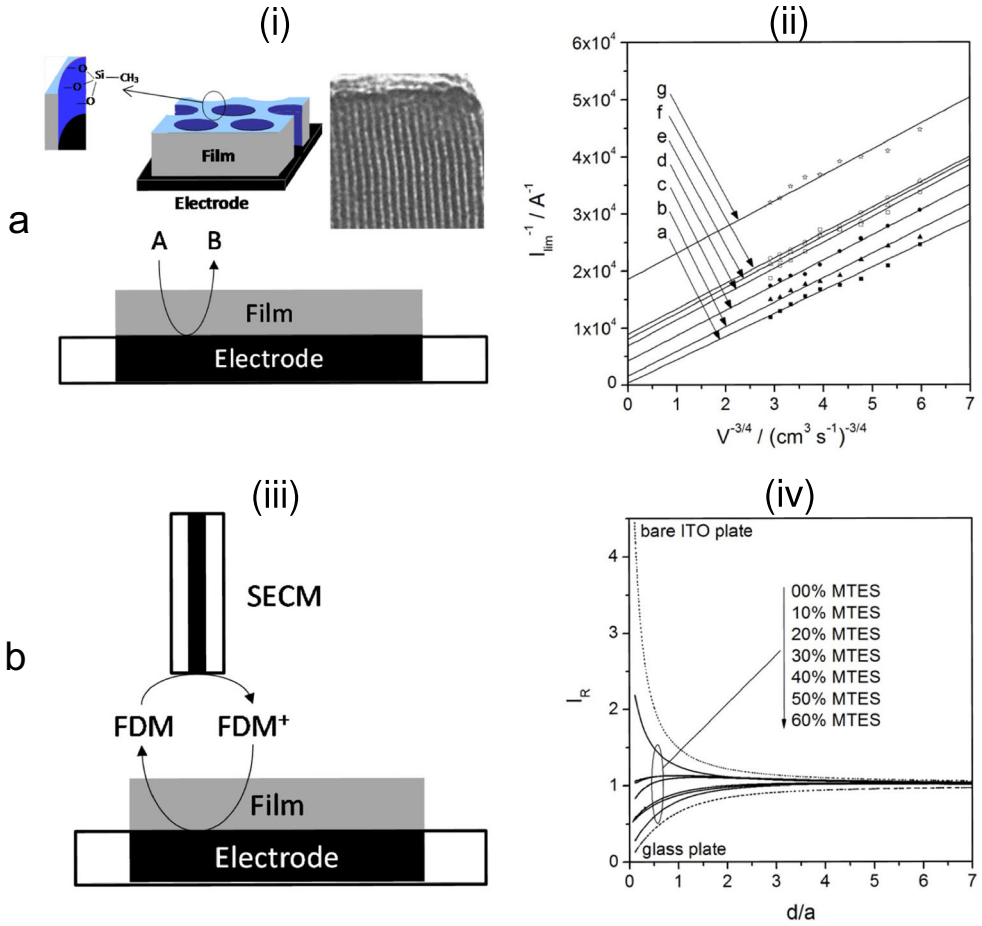

Fig. 14 Quantitative analysis of transport issues in oriented mesoporous silica films bearing increasing amounts of methyl groups (prepared on ITO using various mol percent of methyltriethoxysilane (MTES) in the synthesis medium, as analyzed by WJC **a** and SECM **b**. Schematic representation of the investigated system (***i***). $1/I_{lim}$ versus $V^{-3/4}$ plots (***ii***) obtained from chronoamperometry experiments performed at a potential of 0.8 V versus an Ag/AgCl reference electrode in 0.05 mol L^{-1} potassium hydrogen phthalate solutions containing 1 mM FcEtOH (*a*–*g* correspond respectively to films prepared from sols containing 0 (*a*), 10 (*b*), 20 (*c*), 30 (*d*), 40 (*e*), 50 (*f*), and 60 % (*g*) MTES). Schematic drawing of the SECM experiment (***iii***). Ferrocenedimethanol ($Fc(MeOH)_2$, noted as *FDM* on the figure) is oxidized at the microelectrode, and the ferricinium ions can be regenerated at the larger electrode modified with a porous film only if the species can diffuse through the film and access to the electrode/film interface. Experimental SECM approach curves (***iv***) recorded with a 25-μm-diameter Pt ultramicroelectrode (UME) approaching ITO plates modified with surfactant-extracted methyl-functionalized mesoporous silica thin films. Current variations (i.e., normalized currents and IR, plotted as a function of the normalized UME–substrate distance, *d/a*) were measured by using 1 mM $Fc(MeOH)_2$ as the redox probe in a 0.05 mol L^{-1} potassium hydrogen phthalate solution. The tip voltage was held at +600 mV and ITO substrates were biased at 0 mV versus a silver wire pseudo-reference. Reprinted in part with permission from Guillemin et al. [152]. Copyright 2010 Royal Society of Chemistry

functionalized and oriented mesoporous silica films" section for detail on functionalization). Taking into account that currents measured on the electrode surface (I_{lim}) are limited by mass transport in solution and by the film permeability, the electrode response will be dominated by the film permeability (I_{perm}) for high convection. A Koutecky-Levich plot of $(I_{measured})^{-1}$ versus $(flux)^{-3/4}$ for WJC or versus $(rotation\ speed)^{-2}$ for RDE allows to estimate I_{perm} (see Fig. 14 (ii) for typical plots). The terms of the corresponding relation (Eq. 6) are *d*, the film thickness; *n*, the number of exchanged electrons; *F*, the Faraday constant; *A*, the electrode surface area; *C*, the concentration of redox probe in the solution; *P*, the partition coefficient between the film and the solution; and D_f, the diffusion coefficient of the probe into the film:

$$\frac{1}{I_{lim}} = \frac{1}{I_{perm}} = \frac{d}{nFA(PD_f)c} \quad (6)$$

As shown, more and more restricted mass transport for the redox probe was observed as higher was the methyl group content in the material, due to less and less available space in the mesopore channels for ferroceneethanol species to diffuse. From these data, it is possible to extract permeability values, and they were found to decrease from 1×10^{-7} to 3×10^{-10} cm^2 s^{-1}, from 0 to 60 % methyl group content,

respectively [152]. A similar trend was observed using SECM (see scheme of the method principle in Fig. 14 (iii) and typical data in the form of approach curves in Fig. 14 (iv)). In this case, the film is immersed in a solution containing the probe (ferrocene dimethanol in this case) and an ultramicroelectrode (UME) is approaching the surface, resulting in significant feedback currents only if the molecular probe could diffuse through the film and access to the electrode/film interface [147].

Strategies to get functionalized and oriented mesoporous silica films

Beside the development of oriented mesostructures with vertical channels, another key challenge in mesoporous thin films is their functionalization while maintaining accessible the selected surface groups. Basically, post-grafting could be applied, but it can lead to dramatic blocking effects when used to non-interconnected small mesopore channels oriented normal to the underlying support, as a result of anarchical polycondensation of the organosilane reagents due to the presence of residual water in the pore channels (i.e., pores completely filled with water of above 60 % humidity [147]). This was notably the case of mesoporous silica films generated by EASA and subsequently grafted with aminopropyltriethoxysilane (APTES), which remained blocked to external reagents (such as $Ru(bpy)_3^{2+}$) even when the films were subjected to heat and/or vacuum treatment(s) prior to grafting [153]. The only (partially) successful cases of grafting without totally blocking mass transport through the film are the methyl- [153] or hydroquinone-functionalized ones [154]. In addition, the functionalization of mesoporous materials by post-synthesis grafting is characterized by non-homogeneous spatial distribution of the organofunctional groups (i.e., more groups located at the mesopore entrance than deeper in the material) [155]. It is thus necessary to develop other effective approaches for the functionalization of such oriented mesoporous films.

A first alternative strategy is the electrochemically assisted deposition associated to the self-assembly cocondensation of alkoxysilane and organosilane in mixture to grow in one-step functionalized and vertically aligned mesochannels. It worked quite well, but this was restricted to rather "simple" organofunctional groups (i.e., methyl [152], amine [151, 156], ethylenediamine [157], and thiol [139, 158]), whereas attempts made with more sophisticated organosilanes (e.g., bearing ferrocene or cyclam derivatives [159]) failed due to lack of mesostructuration and/or orientation or phase separation, except for a very recent example of a hydroquinone-linked alkyltriethoxysilane derivative [154]. Nevertheless, applying sol-gel cocondensation in electrochemical interfacial surfactant templating is only possible up to a certain level of organofunctional group loading: For hybrid films prepared by EASA, the ordered mesostructure and pore orientation was maintained for molar ratios of organosilane to TEOS of up to 60 % for methyl groups [152], 10 % for amine [151, 156] and thiol moieties [139], and 8 % for ethylenediamine [157]. Above these values, the transient surfactant hemimicelle assemblies on the electrode surface under potential control are thought to be disturbed and cannot properly induce the growth of an ordered and oriented mesostructure. These grafted organic groups can be further exploited to attach other functions to the material, according to a two-step post-synthesis derivatization process, as firstly demonstrated for hydroquinone derivatives [154, 156]. Note that the way in which the functionalization was performed is likely to affect the properties/reactivity of the resulted hybrid films. This has been pointed out by Rafiee et al. [154] who compared the behavior of hydroquinone-functionalized oriented mesoporous silica films as obtained either by direct grafting of an hydroquinone-linked alkyltriethoxysilane derivative to preformed mesoporous silica, or by its cocondensation with TEOS in the presence of the surfactant template, or by the post-derivatization of amine-functionalized silica films with a suitable dioxopyrrolidin-hydroquinone-based reagent (see corresponding schemes in Fig. 15a, with the corresponding SGAH, AGSH, and CAPH acronyms for the three materials). As shown (Fig. 15b), the electrochemical response of the incorporated hydroquinone moieties significantly depends on the functionalization method (in terms of both voltammetric peak currents and difference of anodic to cathodic peak potentials), leading to a better performance for the material prepared by the one-step cocondensation (CAPH), then the derivatized amino-film (AGSH), and finally the material obtained by grafting (SGAH). A possible explanation to this series is the more uniform distribution of the electroactive groups in the material when passing from SGAH to AGSH and to CAPH. Differences in operational stability were also observed by cyclic voltammetry (i.e., 40 % loss and then fairly stable currents over the day for SGAH, and slight and continuous decrease of currents for all the day for CAPH (12 % loss after 5 h), while the best stability was for AGSH (only 3.7 % loss after 3 days)) [154].

Another alternative strategy, which was recently proposed as a versatile platform toward hybrid films with perpendicular mesochannels, is the electrochemically assisted generation of highly ordered azide-functionalized mesoporous silica combined to subsequent "click chemistry" [153]. The synthesis method (Fig. 16a, top) involves the use of a hydroalcoholic sol containing both TEOS and (3-azidopropyl)trimethoxysilane (AzPTMS), which were allowed to cocondensate by electrochemical interfacial surfactant templating, giving rise to highly ordered and orientedazide-functionalized mesoporous silica films (Fig. 16b) up to 40 mol% AzPTMS in the starting sol. The azide terminal groups are then likely to react with a variety of organic molecules possessing an alkyne group (e.g., ethynylferrocene, Fig. 16a, bottom), and, thanks to the regular mesostructure of the film and good accessibility to the

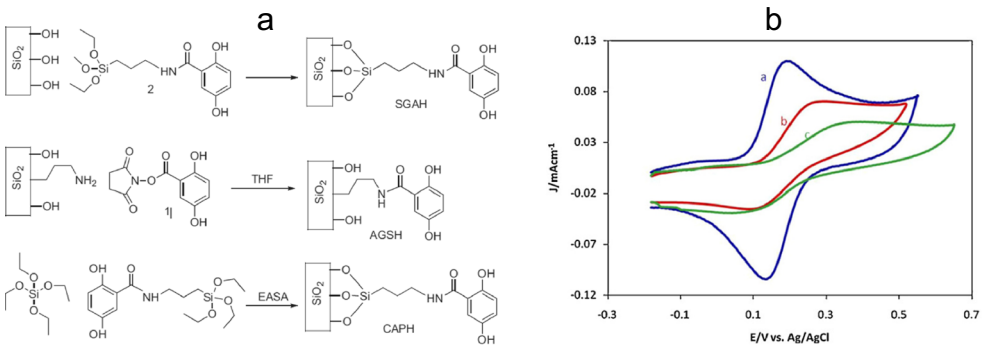

Fig. 15 **a** Scheme illustrating three routes to get EASA-based mesoporous silica films functionalized with hydroquinone moieties: *SGAH* was obtained by post-synthesis grafting of silica with 2,5-dihydroxy-N-(3-(triethoxysilyl)propyl)benzamide(2); *AGSH* corresponds to the cocondensed amine-functionalized silica film derivatized with 2,2'-dioxopyrrolidin-1-yl 2,2'dihydroxybenzoate (1); and *CAPH* is the hybrid film prepared in one step by EASA cocondensation of 2,5-dihydroxy-N-(3-(triethoxysilyl)propyl)benzamide and TEOS. **b** Corresponding cyclic voltammograms recorded using glassy carbon electrodes covered by CAPH (*a*), AGSH (*b*), and SGAH (*c*) in blank phosphate buffer solution at pH 7; scan rate 100 mV s^{-1}. Reprinted with permission from Rafiee et al. [154]. Copyright 2013 Elsevier Ltd

azide groups, a very high yield of functionalization can be achieved [153]. The successful ferrocene grafting is demonstrated through the well-defined voltammetric curves, exhibiting peak currents growing continuously with the azide loading for AzPTMS/TEOS ratios in the range 2.5:97.5 to 40:60, which were stable upon multiple successive potential scanning (Fig. 16c). Consistent with observations made on hydroquinone- or catechol-functionalized films [152, 154], the charge transfer mechanism is most probably electron hopping between adjacent redox sites, explaining the absence of response for too low ferrocene contents (<2.5 %) [153].

Some applications

The field of electrogenerated mesoporous silica films, and especially that of their functionalized forms, is still in its infancy, but some possible electrochemical applications start

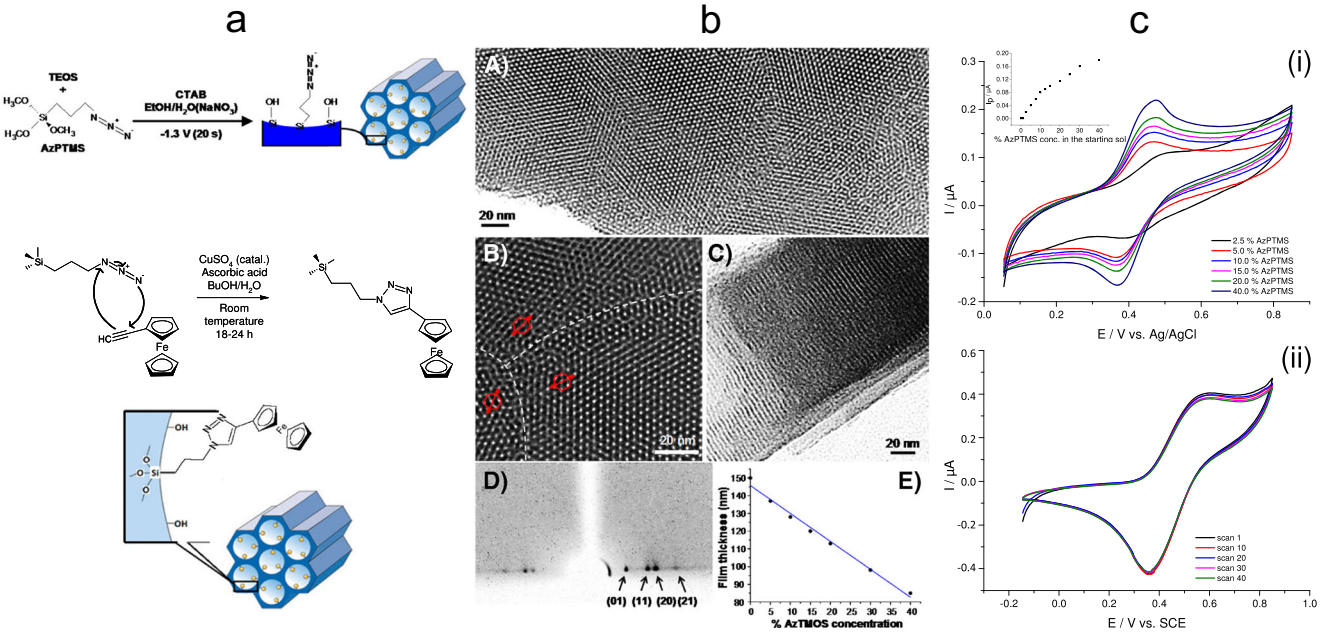

Fig. 16 **a** Illustration of the EASA cocondensation process of AzPTMS and TEOS in the presence of CTAB to get vertically aligned azide-functionalized mesoporous silica film, and the mechanism involved in a typical Huisgen reaction between AzPTMS and the ethynylferrocene. **b** TEM micrographs of the thin film incorporating azide groups obtained from a sol prepared with 20 % AzPTMS (molar ratio relative to the total precursor content): top view (*inset A*) and magnified top view (*inset B*) TEM micrographs, cross-section view (*inset C*), GIXRD pattern (*inset D*), and variation of the film thickness as a function of the % AzPTMS (*inset E*). **c** cyclic voltammograms recorded at 20 mV s^{-1} using ITO electrodes covered with a ferrocene-functionalized film in acetonitrile (+0.1 M $TBAClO_4$) for films prepared from various AzPTMS:TEOS ratios (***i***); multisweep cyclic voltammograms recorded in the same conditions using the 10:90 AzPTMS:TEOS film: 1st, 10th, 20th, 30th, and 40th cycles (***ii***). Reprinted with permission from Vilà et al. [153]. Copyright 2014 WILEY-VCH Verlag GmbH & Co. KGaA

to emerge. They mainly include electroanalysis and the preparation of nanowires.

The fast mass transport rates in such ordered and oriented mesostructures was first exploited in preconcentration electroanalysis. For instance, amine-functionalized and oriented mesoporous silica thin films can be applied to the voltammetric analysis of Cu^{2+} ions subsequent to their open-circuit accumulation thanks to the complexing properties of amino groups toward copper species (Fig. 17a), exhibiting clear advantage of the templated and oriented films in terms of sensitivity (Fig. 17b) due to faster mass transport through the film [151]. Similarly, thiol-functionalized films generated by EASA on ultramicroelectrodes (Pt microdiscs) have been applied to the preconcentration electroanalysis of mercury (II) species [158]. Note that unmodified and unextracted surfactant-templated silica films can be directly applied to the preconcentration and subsequent electrochemical detection of hydrophobic analytes that are likely to accumulate by solubilization into the liquid crystalline phase of the film [160]. On the other hand, catechol-modified films exhibited electrocatalytic properties with respect to NADH [156]; those bearing cobaltammine complexes were applied to the electrocatalytic reduction of hydrogen peroxide [157], while hydroquinone-functionalized films were used for the electrocatalytic oxidation of benzyl alcohol and hydrazine [154], with possible applications in sensing or biosensing. Finally, a recent work has demonstrated the possible electroassisted generation of clay-mesoporous silica composite films on electrodes by combining the EASA process to spin-coated clay films [161]. This was achieved by depositing first the clay particles onto the electrode surface and then generating the mesoporous silica film through the void volume between the clay particles, leading to a composite material exhibiting stronger mechanical stability owing to the presence of the silica binder. After surfactant removal, the resulting materials kept the pristine properties of the clay (i.e., cation exchange) and exhibited excellent permeability issues and long-term mechanical stability, which was notably exploited in preconcentration electroanalysis of copper ions. A particular feature of the developed preparation method was the reversible intercalation/exchange of the cationic surfactant in the interlayer region of the clay, ensuring fast mass transport through the composite film by creating high porosity upon surfactant extraction [161].

The ordered and oriented mesoporous silica films produced by EASA can be basically used as a mold for the electrodeposition of nanoobjects, hopefully in the form of nanowires of extremely narrow diameter. A first attempt was to electrogenerate Prussian Blue (PB) inside such nanochannels [150]. Indeed, pulsed chronoamperometry enabled well to get nanosized PB, as testified by the very small peak-to-peak separation (10 mV) observed for anodic and cathodic counterparts by cyclic voltammetry, but the direct observation of

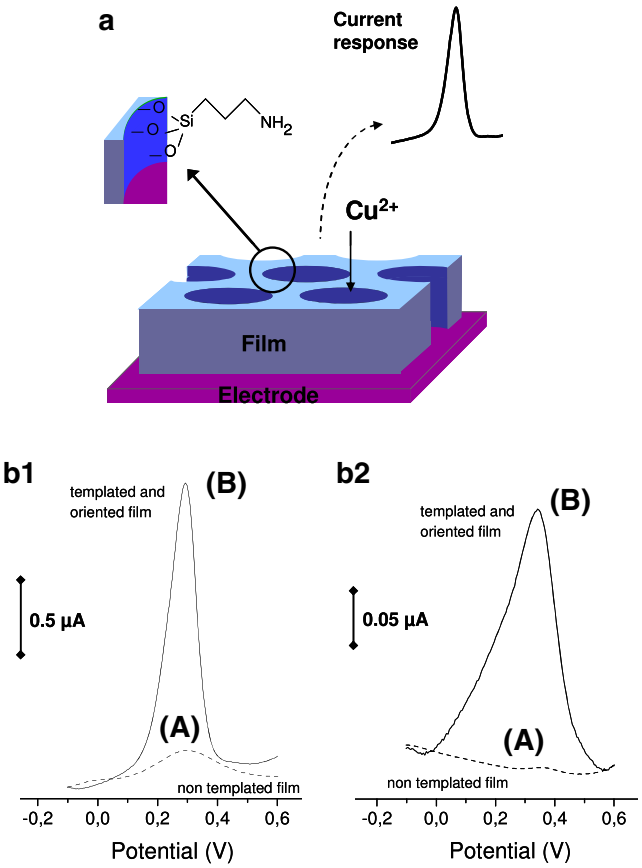

Fig. 17 **a** illustration of the principle of preconcentration electroanalysis of Cu^{2+} at an amine-functionalized and oriented mesoporous silica thin film modified electrode. **b** Typical voltammetric responses obtained for the analysis of 1×10^{-6} M Cu^{2+} (**b1**, 2-min accumulation) and 1×10^{-8} M Cu^{2+} (**b2**, 15-min accumulation) at electrodes respectively modified with a non-templated (*A*) and a templated and oriented (*B*) mesoporous silica film bearing amine groups. Reprinted with permission from Etienne et al. [151]. Copyright 2009 American Scientific Publishers

any small nanowires in the silica mesochannels was not possible by electron microscopy and the presence of PB was only evidenced through energy-dispersive X-ray (EDX) analysis. Conducting polymers have been also electrogenerated in vertically aligned mesoporous films, such as polypyrrole [162] or polythiophene [163]. For polythiophene, for instance, nanowire clusters can be observed by TEM after mechanical removing of polymer fragments from the electrode surface (Fig. 18a), but the single nanowire diameter (i.e., 5.7 nm, Fig. 18b) was larger than that of the mesopore channels (2–3 nm), suggesting possible growth out of the mesoporous silica film. Such composite electrode can be subsequently modified by platinum nanoparticles, and the resulting polythiophene nanowire/platinum nanoparticle system was effective for the electrocatalytic oxidation of formic acid [164]. Polypyrrole nanowires embedded in the mesoporous silica exotemplate were found to exhibit a reversible redox activity [162]. Palladium nanorods were otherwise electrodeposited in oriented mesoporous silica, and the resulting Pb

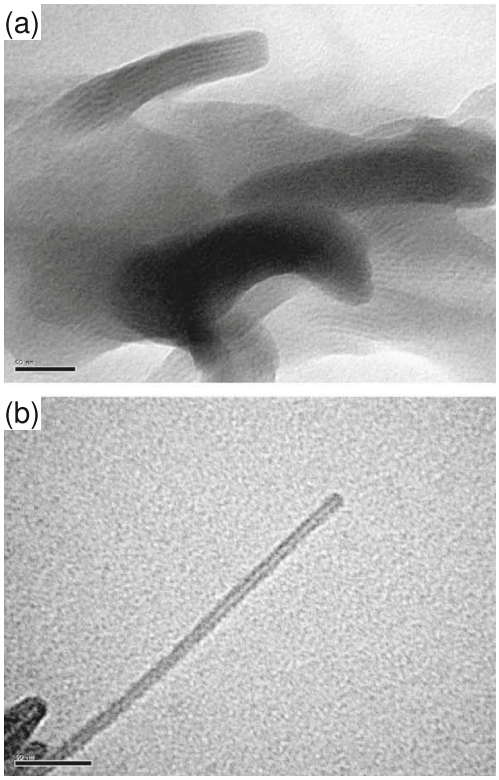

Fig. 18 TEM micrographs of polythiophene electrodeposited in oriented mesoporous silica thin film modified glassy carbon electrode (*top image* shows a fragment of the film and the *bottom* one a single nanowire). Reprinted with permission from del Valle et al. [163]. Copyright 2009 Elsevier Ltd

nanorod array/sol-gel silica thin film electrode was applied to the non-enzymatic detection of glucose and the simultaneous determination of dopamine and uric acid in the presence of ascorbic acid [165]. Finally, hydrophobized oriented mesoporous silica substrates were exploited for the generation of confined fullerene wires that were physically casted into the mesochannels, and it was shown that such dynamically confined fullerene wires allow capacitive diffusion of electrons [166].

Electrogeneration of layered double hydroxides

Among non-silicate compounds, layered double hydroxides (LDH) are two-dimensional solids with positively charged brucite-like layers of mixed metal hydroxides separated by intercalated hydrates anions (Fig. 19). These layered inorganic materials, often called synthetic anionic clays or hydrotalcite-like compounds, can be defined by a chemical formula $[M(II)_{1-x}M(III)_x(OH)_2]^{x+}[X^{q-}_{x/q}\cdot nH_2O]$ where metal cations M (II) are typically Mg, Zn, Ni, Co, Cu; M(III) Al, Cr, Fe, and X^{q-} is the interlayer anion compensating the positive charge of the metal hydroxide layers. Their synthesis, properties, and

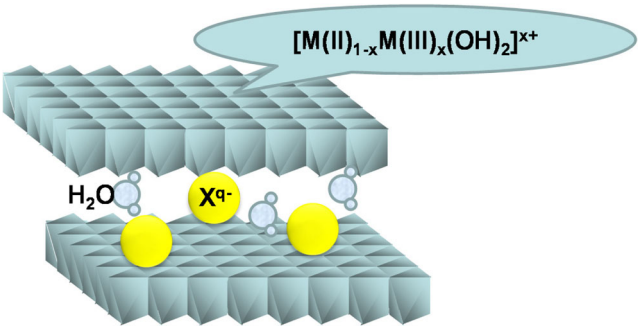

Fig. 19 Schematic representation of layered double hydroxides

applications are well documented in several books and review articles; see for instance Forano et al. [167] and Costantino et al. [168]. In particular, various methods are described in the literature to allow the preparation of LDH with tailored chemical compositions, physical properties, and morphologies depending on their suitable applications. However, among this literature, no recent feature article reports on the synthesis pathway based on the electrogeneration of hydroxide ions at the working electrode as an alternative route to the LDH syntheses. This is the purpose of the present review article, as well.

In the 1990s, Kamath's group realized a pioneer work on the electrochemically induced precipitation (EIP) of bulk samples of LDH containing Ni(II) or Co(II) and Al, Cr, or Fe trivalent metal cations [46, 169, 170]. All the samples were synthesized in a one-step process by cathodic reduction of nitrate ions from a mixed-metal nitrate solution having a M (II)/M(III) molar ratio fixed at 3:1. The same procedure was also applied to prepare MgAl-LDH [170]. It should be noted that LDH cannot be obtained using perchlorate as reduced anion. The electrolysis was carried out for 4 h at 24–26 °C galvanostatically at a current density of 65 mA cm^{-2} using a Pt electrode as working electrode. Nitrate-intercalated LDH materials were recovered as polycrystalline powders by filtration. However, these authors suggested that at low current densities (<1 mA cm^{-2}), thin films could be deposited on the working electrode surface.

For many applications, LDH must form homogeneous supported thin films, for instance, for electrochemical devices like sensors, biosensors, biofuel cells, supercondensators, electrocatalysts, electrochromic, or anticorrosion coatings. There are two different ways to prepare LDH films: deposition on a support or in situ growth on a support [11, 171]. The former is a "two-step method" in which a LDH suspension is first prepared and then coated on a support by means of solvent casting or by "layer-by-layer assembly." The latter is a "one-step method" where the support may be a source of metal cations which are incorporated in the LDH structure during a slow coprecipitation process using urea or ammonia as a precipitant agent. Hence, electrochemically induced precipitation (EIP) may be an alternative to this one-step method

using the electrode as the support where electrogenerated hydroxide anions are used as precipitant agent.

Electrodeposition of LDH thin films

Scavetta et al. have extensively studied the electrodeposition of NiAl-LDH [172] and CoAl-LDH [173, 174] as thin films, mainly on Pt electrode. Nitrate electrolysis is carried out under potentiostatic conditions (E_{app}=−0.9 V/SCE) for various deposition times ($10 \le t_e \le 120$ s) using a mixture of 0.03 M M(II)/Al nitrate salts (3:1) in 0.3 M KNO_3 as plating solution. Under this condition, reproducible, homogeneous, and mechanically stable films of LDH cover the electrode surface [172]. The film thickness increases when the deposition time increases; the mean value ranges from 100 nm for 10 s to 750 nm for 120 s. All the films, even those prepared for very short times, display a M(II)/M(III) molar ratio close to 2 (as determined by EDX), which is compatible with the formation of LDH structure. In the first stages of the potential pulse, there is a linear relation between the mass increase, determined by electrochemical quartz crystal microbalance (EQCM), and the cathodic charge passed during the electrolysis process. These authors suggest that as soon as the cathodic potential is applied to the electrode, direct precipitation of the LDH phases occurs without a previous precipitation Al hydroxides. More recently, LDH with other chemical compositions have been also prepared by EIP, namely, ZnAl [175], MgAl [176, 177], NiFe [178], and MnAl [179]. In all cases, a special attention must be paid to the M(II)/M(III) ratio present in the electrolyte solution, the pH of the solution, the applied potential, and the electrolysis time to ovoid the formation of impurities in the films (i.e., aluminum hydroxide) and obtain well-crystallized LDH films. It should be noted that increasing or decreasing the Al concentration in the plating solution resulted in the formation of Al or Zn containing impurities, instead of varying Al content within the ZnAl-LDH phase [175]. Moreover, the total concentration of nitrate salts in the electrolyte solution seems to play a key role in the final composition and homogeneity of the LDH phases [172]. Interestingly, the electrodeposition of Co(II) nitrate solution at 60 °C using nitrite as hydroxide precursor generates a mixed valence Co(II)Co(III)-LDH [180]. The Co(II) cations are partially oxidized to Co(III) by nitrite under high pH condition generated at the vicinity of the electrode surface. Finally, $Co_xNi_yAl_{0.25}$ layered triple hydroxides ($0.31 \le x \le 0.75$ and $0 \le y \le 0.49$) with anisotropic morphology were synthesized by EIP on stainless steel electrodes [181].

The electrode nature and its surface roughness can also modify the EIP process. For instance, nitrate reduction occurs at lower overvoltage at Pt electrode previously submitted to an electrochemical pretreatment in H_2SO_4, thus affecting the kinetics of precipitation of CoAl films and consequently the film thickness [182]. EIP of LDH can also be realized on other conductive materials, i.e., glassy carbon [178, 183, 184], ITO [185–187], gold films [175] or gold electrode [188, 189], and FeCr alloy foam [177, 190, 191] and stainless steel [181].

NiAl and CoAl LDH thin films obtained under EIP conditions are generally poorly crystalized probably because of the fast kinetics of the LDH precipitation [172, 174, 192]. In order to record X-ray diffractograms (XRD), the electrodeposition process was repeated several times and powder was scratched from Pt electrode. XRD patterns of these samples are consistent with the formation of LDH with a low crystallinity (Fig. 20). They can be indexed in a hexagonal lattice (R-3m space group), and the position of the first 003 and 006 diffraction lines situated in the low angle region (2θ), which is related to the interlamellar distance, is compatible with nitrate-containing LDH. The same basal spacing is reported by Yarger et al. for ZnAl-LDH films [175] and Prasad et al. for MgAl-LDH thin films [176]. Elemental analysis (EDX) is used to confirm that these films do not contain amorphous impurities that cannot be detected by XRD. M(II)/M(III) ratio is scrutinized; this ratio must be within the most reliable limit to form a LDH structure [172, 174, 175]. Under the optimized conditions, these ratios are 1.6 or 2 for ZnAl, NiAl, and CoAl, respectively [172, 174, 175]. Vibrational spectroscopies, namely, FTIR and Raman, confirm the formation of nitrate-intercalated LDH phases [172, 174, 175, 192].

SEM images of NiAl and CoAl LDH films shows dense and homogeneous films of ill-defined LDH particles with a random orientation [174, 192]. However, the time of electrodeposition has a great effect on the film morphology, as shown with high magnified images of NiAl-LDH films (Fig. 21). After 60 s of electrolysis, a homogeneous film with dispersed mesopores is formed with interconnected nanoparticles of 50 nm. When the

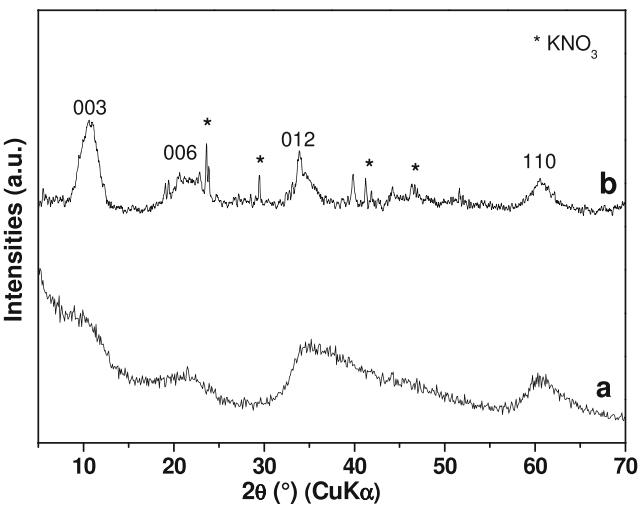

Fig. 20 Powder XRD patterns of **a** NiAl-LDH and **b** CoAl-LDH prepared by electrochemically induced precipitation. Adapted from Scavetta et al. [174] and Khenifi et al. [192], Copyright 2009 and 2012, with permission from Elsevier Ltd

time is further increased ($t_e \geq 120$ s), the film growth continues in a perpendicular direction to the electrode surface and the LDH platelets tend to aggregate together in pseudo-spherical secondary particles. For a longer time (t_e=200 s), the particles become very similar to that obtained for NiAl-LDH prepared by coprecipitation with a sand-rose-like morphology. Interestingly, a 3D nanostructured macroporous NiAl-LDH films can be obtained by an EIP through colloidal crystal of polystyrene beads self-assembled on a Pt electrode which is used as sacrificial template (Fig. 22) [193]. This well-organized colloidal crystal serves as a template during the electrodeposition process. EIP method presents the advantage to fill the template from the bottom up (electrode surface) to the top of the template, limiting the unfilled domains. Finally, the polystyrene beads are removed by dissolution in toluene to give a 3D NiAl-LDH structure.

Electrodeposition of LDH composites

Composite materials based on electrogenerated LDH have been also described in the literature, exploring the multifunctional properties of various building blocks with those of LDH. For instance, many efforts have been devoted recently on the development of hierarchical nanocomposites based on the combination of LDH and nanocarbons [194]. Interestingly, LDH-decorated graphene nanosheets (GNs) have been prepared by one-step EIP processes [184, 195]. In the first example, a glassy carbon electrode (GCE) was first coated with exfoliated graphite oxide (GO/GCE). Then, this electrode was immerged in a Ni/Al nitrate solution, similar to that described by Scavetta et al. [172], and a potential cycling was applied between 0.1 and −1.4 V/SCE. A concomitant electroreduction of GO to graphene nanosheets (GNs) and NiAl-LDH precipitation occurs at the electrode surface (Fig. 23). Uniform LDH nanoparticles (30 nm) are formed randomly on the graphene sheets. Obviously, the as-prepared modified electrode displays an enhanced electroactive surface area (0.59 cm^2) compared to GNs/GCE (0.39 cm^2) and bare GCE (0.062 cm^2) [184]. In the second example, ZnAl/graphene-modified electrode was prepared under potentiostatic conditions (E_{app}=−1.65 V for 120 s) by soaking directly a pretreated GCE within a solution containing GO and Zn/Al nitrate salts [195]. Unfortunately, in both cases, except SEM images, no further physical characterization is available to confirm the formation of LDH phases. Similarly, NiAl-LDH was also prepared using ordered mesoporous carbon modified electrode (OMC/GCE) [196]. Ordered mesoporous carbon (OMC) is a 3D ordered porous conductive material prepared by using mesoporous silica as template and sucrose as carbon source.

Metal nanoparticles, particularly gold nanoparticles (AuNPs), are a subject of growing interest because of their large field of applications toward catalysis, optic, biology, medicine, and nanotechnology [197]. Among the various supports studied for AuNPs, LDHs have attracted a great deal

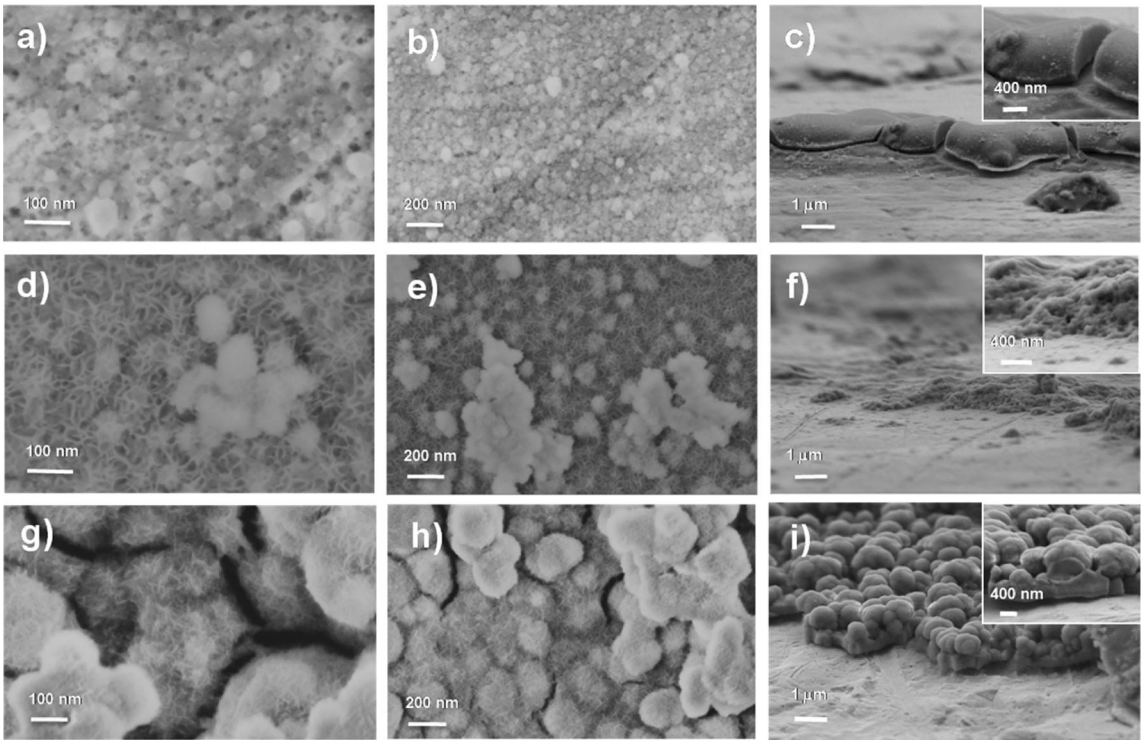

Fig. 21 SEM images of NiAl-LDH thin films for electrodeposition times of 60 s (**a**–**c**), 120 s (**d**–**f**), and 200 s (**g**–**i**). Reprinted from Khenifi et al. [192]. Copyright 2009, with permission from Elsevier Ltd

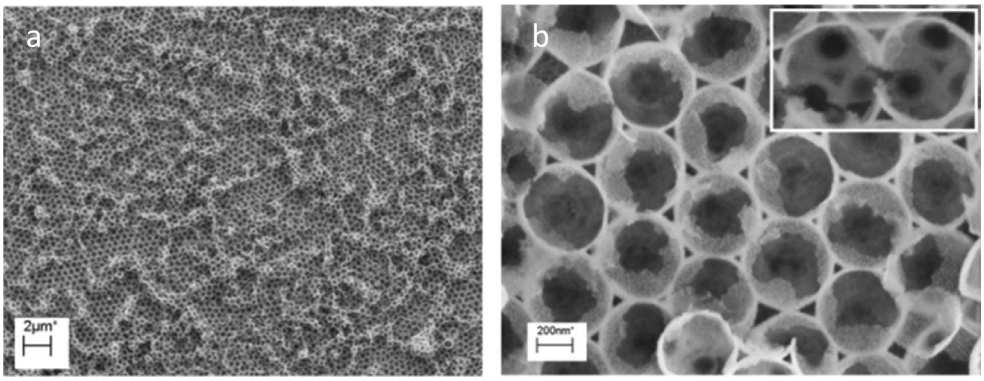

Fig. 22 SEM images of macroporous NiAl-LDH thin film prepared by electrochemically induced precipitation. Adapted with permission from Prevot et al. [193]. Copyright 2011, Royal Society of Chemistry

of interest in recent years [198]. Preparation of heterostructures associating noble metal nanoparticles (AuNPs or PtNPs) and NiAl-LDH are reported by Mignani et al. [185], Wang et al. [199], and Scavetta et al. [200]. Two-step procedures were proposed by Scavetta et al. for PtNPs [200] and by Wang et al. for AuNPs [199]. GCEs are first modified with those Pt or Au nanoparticles, and then, NiAl-LDH films are electrochemically generated on the modified electrodes, leading to uniform coverage of the metal nanoparticles. The opposite procedure was also proposed [201]. A NiAl-NO_3/GCE electrode, prepared by EIP, was immersed into a K_2PtCl_6 solution to allow the accumulation of Pt anionic species within the LDH coating. Electroreduction of exchanged $PtCl_6^{2-}$ anions to Pt(0) was then conducted by CV scanning the LDH-modified electrode in 0.5 M H_2SO_4. However, no physical characterization of the PtNPs/LDH films is provided to prove that the LDH is not dissolved in this so strong acidic condition. Indeed, it is well known that LDH can be easily dissolved in acid medium [202]. Recently, a one-step electrodeposition of AuNPs-NiAl-LDH has been intensively investigated by EQCM [185]. The resulting material was fully characterized by SEM, TEM, UV-Vis, EXAFS, and XANES. It appears that NiAl-LDH and AuNPs grow independently without any mutual interaction at least at distances as close as 3–4 Å, leading to AuNPs with an average diameter of 26 nm and the formal oxidation state of gold of zero. Homogeneous colored thin film of AuNPs-NiAl-LDH was also formed by this method on ITO electrodes having a large geometric surface area (Fig. 24) [185]. Obviously, for easily reducible metals, cation reduction to metal may occur with the hydroxide precipitation. Hence, Rh-based catalyst was prepared by using as precursor an electrogenerated Rh/MgAl-LDH composite [191]. Finally, a two-step electrodeposition method was also conducted to form nickel hexacyanoferrate on NiAl-LDH films [188].

So-called biohybrid materials consist in the association biological materials with inorganic components. Among the variety of inorganic materials available to act as host matrices for biomolecules, LDHs appear as attractive materials. For instance, two main strategies have been developed to immobilize enzymes within LDH [203]. The first one is based on the use of pristine LDH precursors for their ability to adsorb enzymes. The second route takes advantages of the soft chemical conditions used to prepare LDH directly in the presence of the biomolecules. In this context, immobilization of glucose oxidase (GOx) [204, 205] has been achieved during NiAl-LDH EIP at a Pt rotating disk electrode. The as-prepared GOx/LDH-modified electrodes were used as glucose biosensors, and the experimental conditions, i.e., enzyme concentration and Ni/Al molar ratio in the plating solution, have been optimized in order to obtain the best biosensor performance with a good reproducibility [205]. However, enzyme loading on the electrode surface remains quite low (40–80 μg cm^{-2}), and to avoid enzyme leaching, these bioelectrodes are submitted to a chemical crosslinking with glutaraldehyde vapor. Other stabilizing membranes were also tested, i.e., Nafion, titania gel, and Pd hexacyanoferrate hydrogel [206]. Interestingly, scanning electrochemical microscopy (SECM) has been successfully applied to detect the activity of the entrapped enzyme and to obtain topographic images of the bioelectrodes

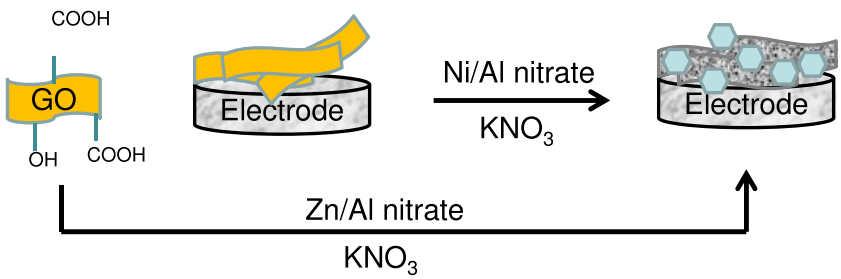

Fig. 23 Procedures for the preparation of GNs/LDH composites by the electrochemically induced precipitation

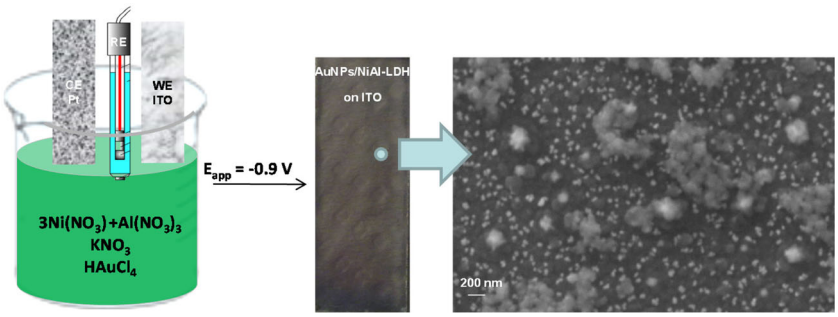

Fig. 24 Procedure for the preparation of AuNPs@NiAl-LDH composite on ITO electrode by electrochemically induced precipitation and the corresponding SEM image

[207]. AFM and SECM images show that GOx distribution is not homogeneous all over the electrode surface, and X-ray photoelectron spectroscopy (XPS) analysis highlights the crucial role played by Ni in GOx immobilization [208]. This fact is confirmed when one compares the amount of GOx entrapped in NiAl-LDH and $Ni(OH)_2$ during EIP process. $Ni(OH)_2$ is able to immobilize a higher amount of biomolecules (188 against 76 μg cm^{-1}) [209]. Furthermore, a two-step procedure was also applied to adsorb GOx and lactate oxidase (LaOx) on normal [210, 211] or macroporous NiAl-LDH-modified electrodes [193]. The analytical performance of these bioelectrodes will be discussed in the "Analytical applications of electrogenerated LDH" section.

Electrochemical characterization

LDH containing transition metal, i.e., Ni(II) and Co(II), can undergo a reversible redox reaction between oxidized and reduced forms of metals, conferring to the LDH-material-specific electrochemical properties, like electrocatalytic or supercondensator properties [212]. Moreover, electrochemical techniques, namely, cyclic voltammetry (CV) and electrochemical impedance spectroscopy (EIS), can be used to deeply characterize redox active LDH to draw some correlations between structural and electrochemical properties [213]. Many efforts have been made by Tonelli's group to study the electrochemical behavior of NiAl [172, 192] and CoAl [173, 174] LDH electrogenerated on Pt electrode. All these films prepared by EIP have been characterized in CV and EIS in NaOH or KOH aqueous solution. During oxidative sweeps, they display electrochromism with a change in color from weakly blue (Ni) or weakly pink (Co) to black. However, this phenomenon is not totally reversible when the potential cycling is stopped.

Typical CV of NiAl-modified electrode displays a reversible signal in the potential window between 0.3 and 0.6 V (Fig. 25). The associated redox process can be described by the following reaction (Eq. 7):

$$\mathrm{Ni(II)-LDH} + \mathrm{OH^-} \rightleftarrows \mathrm{Ni(III)OH-LDH} + 1\mathrm{e^-} \quad (7)$$

The charge transport inside the material is due to a complex mechanism coupling an electron exchange with ion diffusion to compensate the positive extra charge generated upon the faradaic process. Current peak intensity, recorded in CV, increases with the electrodeposition time until 60 s. When the film becomes thicker, the charge transportation is hindered within the film, limiting the proportion of electroactive Ni(II) atoms involved in the electrochemical process. EIS data confirm that the

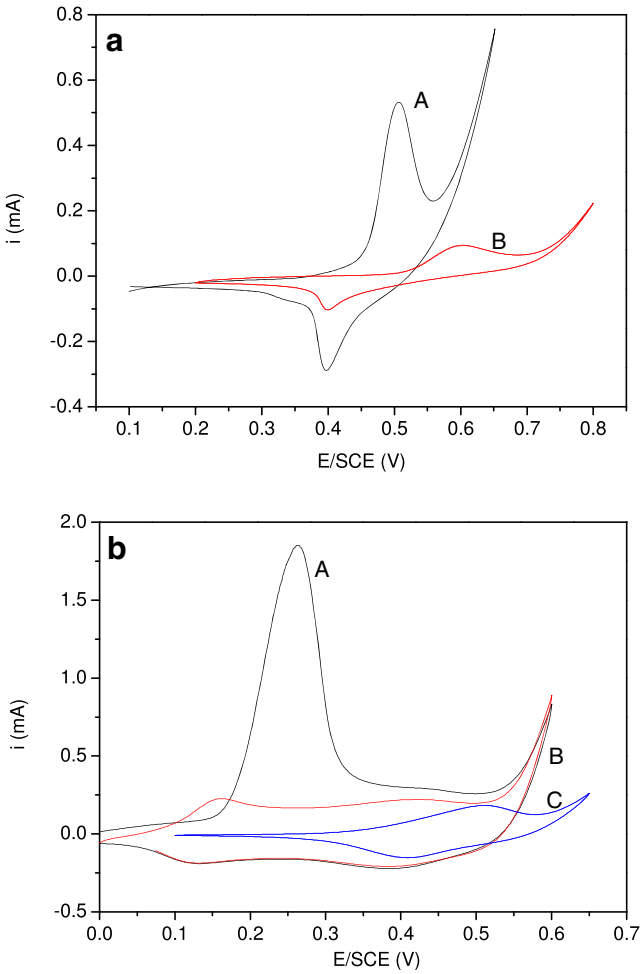

Fig. 25 Cyclic voltammograms of **a** NiAl-NO_3/Pt prepared by electrogeneration (≈35 μg cm^{-2}, 60 s at −0.9 V) (*A*) and by coprecipitation (≈285 μg cm^{-2}) (*B*) in 0.1 M NaOH, v=10 mV s^{-1}; **b** CoAl-NO_3/Pt prepared by electrogeneration (≈60 μg cm^{-2}, 60 s at −0.9 V) first cycle (*A*), second cycle (*B*) and by coprecipitation (≈285 μg cm^{-2}) (*C*) in 0.1 M KOH, v=10 mV s^{-1}

electronic transfer resistance inside the material is affected by the electrodeposition time. Similarly, EIS measurements were carried out with electrogenerated NiAl/Au [189] and ZnAl/GCE [214] in the presence of an electrochemical probe in the electrolyte solution ($K_3Fe(CN)_6$). These results confirm that the longer the electrodeposition, the larger the interfacial electron transfer resistance. An optimal thickness seems to be reached after 60 s. Interestingly, when a NiAl-LDH film is formed under this optimal condition, the resulting cyclic voltammogram displays higher current peak intensities than that obtained for a film of NiAl-NO_3 prepared by solvent casting of a coprecipitated phase (Fig. 25). Indeed, in the former case, the charge transfer (Q_a) involved in the electrochemical oxidation of Ni(II) inside the LDH lattice is sixfold higher than in the latter case, whereas the amount of LDH deposited on the electrode surface is heightfold lower (35 μg cm^{-2} instead of 285 μg cm^{-2}). Moreover, the oxidation peak is situated at a lower potential suggesting a better reversibility of the electrochemical process. An intimate interaction between the electrogenerated NiAl-LDH platelets and the electrode surface seems particularly favorable to the electronic transfer. It should be recalled that the electrochemical behavior of NiAl-LDH phases is the result of competing effects between the coherent domain size versus the particle size, the aggregation state of LDH particles, the Ni bulk concentration, and the presence of structural defects [213].

On the other hand, electrochemical behavior of electrodeposited CoAl-LDH is more complex than that observed for CoAl-LDH prepared by the coprecipitation method. With this material, a stable quasi-reversible signal is observed in CV at a mean potential ($E_{1/2}$= Ep_a+Ep_c/2) of 440 mV/SCE (Fig. 25a) [215]. For CoAl-LDH prepared by EIP, the first scan is dominated by an irreversible anodic peak at 0.26 V/SCE (Fig. 25b). From the second scan, the CV curve evidences two distinct oxidation and reduction peaks between 0.1 and 0.5 V. This current response has a pseudo-capacitive shape which remains unchanged for several hundred of cycles. The corresponding specific capacitance is evaluated to 500 F g^{-1} that makes this material a good candidate for supercapacitor applications. XRD, IR and Raman spectroscopies, and EQCM analysis have been used to study deeper the phase changes occurring when the as-prepared CoAl-LDH thin films were electrochemically oxidized and reduced by cycling the potential between 0 and 0.6 V in KOH [174]. An irreversible phase transformation occurs after the first cycle leading to the formation of a γ-Co_{1-x}AlOOH phase. The two redox processes, observed from the second scan, are in good agreement with the successive formation of β-Co(III)OOH and β-Co(II)$(OH)_2$. A preliminary study describes also the electrochemical behavior MnAl-LDH prepared by electrochemical precipitation [179]. As previously described for CoAl-LDH, an irreversible phase transformation occurs after the first cycle, with the hypothetical formation of a birnessite-like layer material giving rise to well-defined reversible redox peaks situated at −0.2 V/Hg/HgO. The electrochemical response of those LDH materials has been mainly exploited for electrocatalytic determination of various substrates as described in the next section. Some of these materials were used as catalyst precursors, in particular those prepared on metallic foams, to be used for H_2 production [190] and methane oxidation [191, 216].

Analytical applications of electrogenerated LDH

These as-described LDH thin films have found applications as amperometric sensors and biosensors. Indeed, LDH films can adsorb organic molecules; consequently, they have been used for the detection of catechol, hydroquinone, and resorcinol, for instance, by means of adsorptive stripping analysis [195, 214]. The replacement of ZnAl-LDH film by ZnAl/graphene composite improves the sensor performance with an increase of the detection limit for hydroquinone from 1 μM with the first type of electrode to 0.077 μM with the second one [195]. A ZnAl-LDH film was also used for the determination of epinephrine, a catecholamine neurotransmitter, and uric acid in real samples by means of differential pulse analysis [217].

Other analytical devices are mainly based on NiAl-LDH. Indeed, Ni(II)/Ni(III) redox couple inside the LDH lattice has an electrocatalytic activity with respect to the oxidation of alcohols and amines [218]. For instance, for methanol oxidation, NiAl/GCE shows higher electrocatalytic activity and stability than that of electrogenerated Ni hydroxide ($Ni(OH)_2$/GCE) [219]. When target molecules are present in NaOH solution, a catalytic response is evidenced by the increase of anodic peak, relative to Ni(II) oxidation as summarized in the following equations:

$$\mathrm{Ni(II){-}LDH} + \mathrm{OH^-} \rightleftarrows \mathrm{Ni(III)OH{-}LDH} + 1\mathrm{e^-} \quad (8a)$$

$$\mathrm{Ni(III)OH{-}LDH} + \mathrm{Analyte_{Red}} \rightleftarrows \mathrm{Ni(II){-}LDH} + \mathrm{Analyte_{Ox}} \quad (8b)$$

Primary alcohols (i.e., methanol and ethanol) have been first tested as target analytes [183, 220]. Interestingly, NiAl/PtNPs/GCE exhibits a wider linear range for ethanol determination with an upper limit of 65 mM compared to 12 mM for pristine NiAl/GCE electrode

[200]. Similarly, a synergic effect between NiAl-LDH and AuNPs improves the catalytic efficiency toward methanol oxidation [185, 199], opening other perspectives for these composite catalysts, such as in fuel cells. Among the saccharide compounds, the electrochemical determination of glucose has been extensively investigated at electrogenerated NiAl films [183, 189, 220]. An acetylcholine (Ach) sensor based on NiAl/OMC/GCE is also described [196]. Ach is hydrolyzed in alkaline solution to produce acetic acid and choline which can be electrocatalytically oxidized by Ni(II) species within the LDH layers. On the other hand, an amperometric sensor based on NiAl-LDH/Pt has been developed for the electrochemical analysis of two herbicides, namely, gyphostate and glufosinate, using the electrocatalytic properties of this material toward oxidation of amine groups [192]. Gong's group is focused on the determination by striping analysis of another pesticide, methylparathion, using electrogenerated NiAl/GCE [221], PtNPs/NiAl/GCE [201], or NiAl/graphene/GCE [184]. Unfortunately, in all cases, the same detection limit is reported, namely, 0.6 ng ml^{-1}, and no specific electrocatalytic behavior was shown.

The electrocatalytic properties of CoAl-LDH were also studied for alcohol oxidation. Since Co(II) is oxidized at a slightly lower potential than Ni(II), the corresponding LDH does not display catalytic activity toward monohydric alcohols [222]. Consequently, only multifunctional alcohols (i.e., glycerol, monosaccharides, and polysaccharides) can be detected at CoAl-LDH. Interestingly, electrochromism of CoAl/ITO films has been exploited for an optical determination of glucose [187]. Similarly, electrocatalytic properties of electrogenerated NiAl and CoAl coated on GCE have been also compared for H_2O_2 oxidation [186]. NiAl-LDH shows a lower detection limit and a better reproducibility than the CoAl one which displays a wider linear range. CoAl/GCE has been also used as a pH sensor [223]. Determination of aniline and phenol was also quantified using CoAl/Pt-modified electrode. It appears that electrochemical pretreatment of underlying Pt electrode can improve the analytical performance, preventing electrode passivation [182]. Finally, CoAl-LDH film has been also employed to quantify salicylic acid as an impurity in pharmaceutical samples containing acetyl salicylic acid [224].

Very recently, NiFe-LDH was prepared by the electrochemical method. This material displays two redox peaks situated at 0.8 and −0.6 V, attributed respectively to Ni(II)/Ni(III) and Fe(II)/Fe(III) redox reactions. The redox peak (Fe(II)/Fe(III)) can be applied to the electrocatalytic reduction of metronidazole, a heterocyclic nitro compound used as antibacterial and anticancer agents [178]. Similarly, NiAl-LDH doped with nickel hexacyanoferrate was used for the electroanalysis of ascorbic acid with the help of Fe(II)/Fe(III) redox couple [188].

Amperometric detection of glucose was also extensively reported at GOx/NiAl-LDH biosensors. In this case, the electrochemical response corresponds to the oxidation at the Pt electrode of hydrogen peroxide which is formed in the enzymatic reaction:

$$\text{Glucose} + O_2 \; GO_x \; \text{Gluconolactone} + H_2O_2 \tag{9a}$$

$$H_2O_2 \; Pt \; O_2 + 2H^+ + 2e^- \tag{9b}$$

As previously described ("Electrochemical characterization" section), the parameters of EIP to prepare GOx/NiAl thin films on Pt electrode were optimized to obtain the best glucose biosensor performance [205]. However, the amount of entrapped enzyme remains low; therefore, the sensitivities are low, namely, 7.7 and 19 mA M^{-1} cm^{-2} in batch and flow injection modes, respectively [204]. However, in batch, the sensitivity is improved when GOx is adsorbed on nanostructured NiAl film (13 mA M^{-1} cm^{-2}) [193]. Indeed, the high porosity of the film facilitates the diffusion of glucose and H_2O_2 through the LDH film. Moreover, it was proposed that Ni in the oxidized state can be employed as an anti-interfering system toward ascorbic acid. The effectiveness of GOx/NiAl biosensors has been demonstrated by measuring glucose in fruit juices [210]. Similarly, the determination of lactate in a commercial serum sample was successfully realized with LaOx/NiAl biosensor [211].

Conclusion and outlook

From the examples described in this review, it appears clearly that electrochemically assisted deposition of inorganic materials such as ordered mesoporous silica or LDH films (including their organic-inorganic hybrid or composite forms), by local pH tuning, is a versatile method to generate functional coatings on solid electrode surfaces. In such a way, hydroxide species are produced at the electrode/solution interface (typically in a diffusion layer of approximately 50–500 μm in thickness depending on the electrolysis conditions), and they can be used either to precipitate suitable precursors (e.g., to form LDH-type materials) or to catalyze sol-gel reactions (e.g., to grow surfactant-templated silica films) without requiring the use of bulk solution-phase catalysts. Contrary to evaporation methods (such as dip or spin coating, for which the

material starts to grow from the air/solution interface) or deposition from preformed particles (leading to rather heterogeneous deposits, usually of poor mechanical stability), the approaches described here are based on an interfacial electrochemically induced deposition process for which the material growth starts at the level of the underlying support. The thickness of the deposits can be easily controlled by tuning the electrodeposition parameters and/or the synthesis medium composition, this latter remaining unaffected by the film formation as only the diffusion layer is affected by the electroassisted deposition. On the other hand, the deposition process is dominated by kinetics, which could be an advantage (for instance to get vertically aligned mesoporous silica, which has the tendency to orient parallel to the support when formed by evaporation under thermodynamic control), but also a drawback (leading, for instance, to poorly structured LDH materials as a reason of a too fast electrodeposition). Nevertheless, the method is compatible with the encapsulation of nanoobjects or biomolecules (e.g., to form LDH-based composite or biohybrid materials), and it starts to be developed to generate organically functionalized films (e.g., mesoporous silica-based organic-inorganic hybrids). Although being basically interesting for applications in various fields (protective coatings, permselective membranes, catalysis, hard templates, etc.), these films have been mostly applied to date to electroanalysis and biosensors, but one can anticipate an expansion to other fields in the near future, at least if one could overcome some remaining challenges.

Dealing with ordered and oriented mesoporous silica-based thin films, besides the need for functionalization with organic groups (which starts to be achievable but still has to be extended), a great challenge is to find a way to tune the pore size in a much wider range than only around 2 nm (i.e., up to 5–6 nm would be nice to entrap biomolecules, for instance). Possible strategies are the use of micelle swelling agents or the resort to charged organosilane precursors likely to interact with the oppositely charged micelles to move away the silica walls from each other. Another important point with respect to applications requiring long-term operational stability is the lack of chemical inertness (and consequently poor structural stability) of mesoporous silica in aqueous medium (especially at pH above 7). A way to circumvent this limitation would be the extension of the electroassisted self-assembly method to non-silica materials (e.g., other surfactant-templated metal oxides such as ZrO_2 or TiO_2), or at least to generate mixed mesoporous oxides which could benefit from a synergistic effect of improved chemical stability offered by non-silica precursors and possible functionalization via the organosilane chemistry. Finally, strategies should be developed to get oriented mesoporous materials modified with bifunctional or multifunctional groups in order to further extend their scope of application (notably in catalysis). In the field of electrogenerated LDH materials, the future prospects will be focused on a detailed study of the electrodeposition mechanisms that would allow a better control of composition, structure, and crystallinity of the LDH phases. A challenge would be to follow the growth of the LDH-film by *in operando* methods. Furthermore, the formation of oriented mesoporous phases is very desirable for various applications (i.e., for enzyme immobilization as suggested for silica-based thin films). So far, this approach was only performed with an inverse opal method, but the use of micellar templating agents is not yet explored as it was already done for simple nickel or cobalt hydroxides. Moreover, the use of surfactant or templating molecules having specific properties (electrochemical or magnetic) would allow the formation of hybrid materials with multifunctionalities which can open new opportunities in their application fields, as well.

References

1. Murray RW (ed) (1992) Molecular design of electrodes surfaces. Wiley, New York
2. Walcarius A (2004) In: Nalwa HS (ed) Encyclopedia of nanoscience and nanotechnology, vol 2. American Scientific Publishers, Stevenson Ranch, pp 857–893
3. Walcarius A (1999) Anal Chim Acta 384:1–16
4. Walcarius A (2008) Electronal 20:711–738
5. Muresan LM (2011) Pure Appl Chem 83:325–343
6. Macha SM, Fitch A (1998) Microchim Acta 128:1–18
7. Navrátilová Z, Kula P (2003) Electroanalysis 15:837–846
8. Mousty C (2004) Appl Clay Sci 27:159–177
9. Mousty C (2010) Anal Bioanal Chem 396:315–325
10. Tonelli D, Scavetta E, Giorgetti M (2013) Anal Bioanal Chem 405: 603–614
11. Mousty C, Prévot V (2013) Anal Bioanal Chem 405:3513–3523
12. Walcarius A (2013) Chem Soc Rev 42:4098–4140
13. Yamauchi Y, Kuroda K (2008) Chem Asian J 3:664–676
14. Walcarius A (2012) Trends Anal Chem 38:79–97
15. Hasanzadeh M, Shadjou N, Eskandani M, de la Guardia M (2012) Trends Anal Chem 40:106–118
16. Rao H, Wang X, Du X, Xue Z (2013) Anal Lett 46:2789–2812
17. Etienne M, Walcarius A (2005) Electrochem Commun 7:1449–1456
18. Etienne M, Quach A, Grosso D, Nicole L, Sanchez C, Walcarius A (2007) Chem Mater 19:844–856
19. Wei TC, Hillhouse HW (2007) Langmuir 23:5689–5699
20. Walcarius A, Ganesan V, Larlus O, Valtchev V (2004) Electronal 16:1550–1554
21. Winand R (1994) Electrochim Acta 39:1091–1105
22. Simka W, Puszczyk D, Nawrat G (2009) Electrochim Acta 54: 5307–5319
23. Mohanty US (2011) J Appl Electrochem 41:257–270
24. Plowman BJ, Bhargava SK, O'Mullane AP (2011) Analyst 136: 5107–5119

25. Guo DJ, Ding Y (2013) Electronal 24:2035–2043
26. Beck F (1988) Electrochim Acta 33:839–850
27. Imisides MD, John R, Riley PJ, Wallace GG (1991) Electronal 3: 879–889
28. Zhitomirsky I (2011) Surf Eng 27:1–4
29. Khun AT, Chan CY (1983) J Appl Electrochem 13:189–207
30. Davis J, Cooper JM (2002) J Electroanal Chem 520:13–17
31. Sayen S, Walcarius A (2005) J Electroanal Chem 581:70–78
32. Chen PC, Chen RLC, Cheng TJ, Wittstock G (2009) Electronal 21: 804–810
33. Li Y, Pang X, Epand RF, Zhitomirsky I (2011) Mater Lett 65:1463–1465
34. Therese GHA, Kamath PV (2000) Chem Mater 12:1195–1204
35. Zhitomirsky I (2002) Adv Colloid Interface Sci 97:279–317
36. Chaim R, Stark G, Gal-Or L, Bestgen H (1994) J Mater Sci 29: 6241–6248
37. Seshadi A, de Tacconi NR, Chenthamarakshan CR, Rajeshwar K (2006) Electrochem Solid-State Lett 9:C1–C4
38. Li FB, Newman RC, Thompson GE (1997) Electrochim Acta 42: 2455–2464
39. Chaim R, Almaleh-Rockman S, Gal-Or L (1994) J Am Ceram Soc 77:3202–3208
40. Lee GR, Crayston JA (1996) J Mater Chem 6:187–192
41. Velichenko AB, Amadelli R, Benedetti A, Girenko DV, Kovalyov SV, Danilova FI (2002) J Electrochem Soc 149:C445–C449
42. Peulon S, Lincot D (1996) Adv Mater 8:166–170
43. Pauporté T (2002) J Electrochem Soc 149:C539–C545
44. Dixit M, Kamath PV, Kumar VG, Munichandraiah N, Shukla AK (1996) J Power Sources 63:167–171
45. Pickett DF, Maloy JT (1978) J Electrochem Soc 125:1026–1032
46. Indira L, Dixit M, Kamath PV (1994) J Power Sources 52:93–97
47. Therese GHA, Kamath PV, Subbanna GN (1998) J Mater Chem 8: 405–408
48. Pauporté T, Goux A, Kahn-Harari A, de Tacconi N, Chenthamarakshan CR, Rajeshwar K, Lincot D (2003) J Phys Chem Solids 64:1737–1742
49. Yoshida T, Zhang J, Komatsu D, Sawatani S, Minoura H, Pauporté T, Lincot D, Oekermann T, Schlettwein D, Tada H, Wöhrle D, Funabiki K, Matsui M, Miura H, Yanagi H (2009) Adv Funct Mater 19:17–43
50. Zhitomirsky I, Petric A, Niewczas M (2002) JOM 54:31–34
51. Jiao S, Xu D (2010) In: Umar A, Hahn YB (eds) Metal oxide nanostructures and their applications, vol 2. American Scientific Publishers, Stevenson Ranch, pp 515–540
52. Tong YX, Li GR (2010) In: Umar A, Hahn YB (eds) Metal oxide nanostructures and their applications, vol 5. American Scientific Publishers, Stevenson Ranch, pp 547–579
53. Zeng H, Cui J, Cao B, Gibson U, Bando Y, Golberg D (2010) Adv Mater 2:336–358
54. Shacham R, Avnir D, Mandler D (1999) Adv Mater 11:384–388
55. Deepa PN, Kanungo M, Claycomb G, Sherwood PMA, Collinson MM (2003) Anal Chem 75:5399–5405
56. Sibottier E, Sayen S, Gaboriaud F, Walcarius A (2006) Langmuir 22:8366–8373
57. Collinson MM (2007) Acc Chem Res 40:777–783
58. Sayen S, Walcarius A (2003) Electrochem Commun 5:341–348
59. Walcarius A, Sibottier E (2005) Electroanalysis 17:1716–1726
60. Tan X, Li B, Liew KY, Li C (2010) Biosen Bioelectron 26:868–871
61. Wu LK, Hu JM, Zhang JQ, Cao CN (2013) Electrochem Commun 26:85–88
62. Jiang LL, Wu LK, Hu JM, Zhang JQ, Cao CN (2012) Corros Sci 60: 309–313
63. Nadzhafova O, Etienne M, Walcarius A (2007) Electrochem Commun 9:1189–1195
64. Jia WZ, Wang K, Zhu ZJ, Song HT, Xia XH (2007) Langmuir 23: 11896–11900
65. Rozhanchuk T, Tananaiko O, MazurenkoI E, Etienne M, Walcarius A, Zaitsev V (2009) J Electroanal Chem 625:33–39
66. Bon Saint Côme Y, Lalo H, Wang Z, Kohring GW, Hempelmann R, Etienne M, Walcarius A, Kuhn A (2013) Electroanalysis 25:621–629
67. Ghach W, Etienne M, Billard P, Jorand F, Walcarius A (2013) J Mater Chem B 1:1052–1059
68. Toledano R, Shacham R, Avnir D, Mandler D (2008) Chem Mater 20:4276–4283
69. Raveh M, Liu L, Mandler D (2013) Phys Chem Phys 15:10876–10884
70. Liu L, Mandler D (2013) Electrochim Acta 102:212–218
71. Shacham R, Mandler D, Avnir D (2010) CR Chim 13:237–241
72. Qu F, Nasraoui R, Etienne M, Bon Saint Côme Y, Kuhn A, Lenz J, Gajdzik J, Hempelmann R, Walcarius A (2011) Electrochem Commun 13:138–142
73. Lalo H, Bon Saint Côme Y, Plano B, Etienne M, Walcarius A, Kuhn A (2012) Langmuir 28:2323–2326
74. Mazurenko I, Etienne M, Ostermann R, Smarsly BM, Tananaiko O, Zaitsev V, Walcarius A (2011) Langmuir 27:7140–7147
75. Wang Z, Etienne M, Poeller S, Schuhmann W, Kohring GW, Mamane V, Walcarius A (2012) Electroanalysis 24:376–385
76. Okner R, Favaro G, Radko A, Domb AJ, Mandler D (2010) Phys Chem Phys 12:15265–15273
77. Luna-Vera F, Dong D, Hamze R, Liu S, Collinson MM (2012) Chem Mater 24:2265–2273
78. Lui L, Toledano R, Danieli T, Zhang JQ, Hu JM, Mandler D (2008) Chem Commun 47:6909–6911
79. Schwamborn S, Etienne M, Schuhmann W (2011) Electrochem Commun 13:759–762
80. Ranganathan D, Zamponi S, Berrettoni M, Layla Mehdi B, Cox JA (2010) Talanta 82:1149–1155
81. Liu X, Li B, Wang X, Li C (2010) Microchim Acta 171:399–405
82. Azar PA, Tehrani MS, Mohammadiazar S, Husain SW (2012) J Sep Sci 35:3354–3360
83. Hu JM, Liu L, Zhang JQ, Cao CN (2007) Prog Org Coat 58:265–271
84. Walcarius A, Kuhn A (2008) Trends Anal Chem 27:593–603
85. Walcarius A (2010) Anal Bioanal Chem 396:261–272
86. Etienne M, Walcarius A (2013) In: Compton R, Wadhawan J (eds) Electrochemistry Vol. 11—Nanosystems electrochemistry. The Royal Society of Chemistry, RSC Publishing, pp. 124-197
87. Kresge CT, Leonowicz ME, Roth WJ, Vartuli JC, Beck JS (1992) Nature 359:710–712
88. Beck JS, Vartuli JC, Roth WJ, Leonowicz ME, Kresge CT, Schmitt KD, Chu CTW, Olson DH, Sheppard EW (1992) J Am Chem Soc 114:10834–10843
89. Soler-Illia GJAA, Sanchez C, Lebeau B, Patarin J (2002) Chem Rev 102:4093–4138
90. Wan Y, Zhao D (2007) Chem Rev 107:2821–2860
91. Li W, Yue Q, Deng Y, Zhao D (2013) Adv Mater 25:5129–5152
92. Hoffmann F, Cornelius M, Morell J, Fröba M (2006) Angew Chem Int Ed 45:3216–3251
93. Hoffmann F, Fröba M (2010) In: K. Rurack K, Martínez-Máñez R (eds) The supramolecular chemistry of organic-inorganic hybrid materials. John Wiley & Sons, Inc., Hoboken, NJ, USA, pp. 39-111
94. Chem Soc Rev (2013) Themed issue: Mesoporous materials. In: Lebeau B, Galarneau A, Linden M (eds) 20 years of mesopore control. The Royal Society of Chemistry, RSC Publishing, vol. 42, pp. 3661-4255
95. Lee UH, Kim MH, Kwon YU (2006) Bull Korean Chem Soc 27:808
96. Pénard AL, Gacoin T, Boilot JP (2007) Acc Chem Res 40:895–902
97. Sanchez C, Boissière C, Grosso D, Laberty C, Nicole L (2008) Chem Mater 20:682–737
98. Innocenzi P, Malfatti LA (2013) Chem Soc Rev 42:4198–4216
99. Brinker CJ, Lu Y, Sellinger A, Fan H (1999) Adv Funct Mater 11: 579–585

100. Grosso D, Cagnol F, Soler-Illia GJDAA, Crepaldi EL, Amenitsch H, Brunet-Bruneau A, Bourgeois A, Sanchez C (2004) Adv Funct Mater 14:309–322
101. Innocenzi P, Malfatti L, Kidchob T, Falcaro P (2009) Chem Mater 21:2555–2564
102. Wu KCW, Jiang X, Yamauchi Y (2011) J Mater Chem 21:8934–8939
103. Urbanova V, Walcarius A (2014) Z Anorg Allg Chem (doi: 10.1002/zaac.201300442)
104. Chen M, Burgess I, Lipkowski J (2009) Surf Sci 603:1878–1891
105. Choi KS, Lichtenegger HC, Stucky GD, McFarland EW (2002) J Am Chem Soc 124:12402–12403
106. Choi KS, McFarland EW, Stucky GD (2003) Adv Mater 15:2018–2021
107. Attard GS, Bartlett PN, Coleman NRB, Elliott JM, Owen JR, Wang JH (1997) Science 278:838–840
108. Elliott JM, Attard GS, Bartlett PN, Coleman NRB, Merckel DAS, Owen JR (1999) Chem Mater 11:3602–3609
109. Elliott JM, Attard GS, Bartlett PN, Owen JR, Ryan N, Singh G (1999) J New Mater Electrochem Syst 2:239–241
110. Choi KS, Steinmiller EMP (2008) Electrochim Acta 53:6953–6960
111. Tan Y, Srinivasan S, Choi KS (2005) J Am Chem Soc 127:3596–3604
112. Yarger MS, Steinmiller EMP, Choi KS (2007) Chem Commun 159-161
113. Baeck SH, Choi KS, Jaramillo TF, Stucky GD, McFarland EW (2003) Adv Mater 15:1269–1273
114. Nakayama M, Konishi S, Tagashira H, Ogura K (2005) Langmuir 21:354–359
115. Yuan YF, Xia XH, Wu JB, Gui JS, Chen YB, Guo SY (2010) J Membr Sci 364:298–303
116. Spray RL, Choi KS (2007) Chem Commun 3655-3657
117. Lee CW, Nam KW, Cho BW, Kim KB (2010) Microporous Mesoporous Mater 130:208–214
118. Tan Y, Steinmiller EMP, Choi KS (2005) Langmuir 21:9618–9624
119. Steinmiller EMP, Choi KS (2007) Langmuir 23:12710–12715
120. Xing LL, Xue XY (2010) Solid State Sci 12:1593–1598
121. Elias J, Lévy-Clément C, Bechelany M, Michler J, Wang GY, Wang Z, Philippe L (2010) Adv Mater 22:1607–1612
122. Luo H, Lin Q, Baber S, Naalla M (2010) J Nanomater 2010:3
123. Bruns CJ, Herman DJ, Minuzzo JB, Lehrman JA, Stupp SI (2013) Chem Mater 25:4330–4339
124. Choi KS, Steinmiller EMP, Yarger MS (2007) Mater Res Soc Symp Proc 972:91–96
125. Walcarius A, Sibottier E, Etienne M, Ghanbaja J (2007) Nat Mater 6:602–608
126. Goux A, Etienne M, Aubert E, Lecomte C, Ghanbaja J, Walcarius A (2009) Chem Mater 21:731–741
127. Cheng J, Rathi SJ, Stradins P, Frey GL, Collins RT, Williams SKR (2014) RSC Adv 4:7627–7633
128. Wang X, Xiong R, Wei G (2010) Surf Coat Technol 204:2187–2192
129. Koganti VR, Dunphy D, Gowrishankar V, McGehee MD, Li XF, Wang J, Rankin SE (2006) Nano Lett 6:2567–2570
130. Eggiman BW, Tate MP, Hillhouse HW (2006) Chem Mater 18:723–730
131. Nagarajan S, Li M, Pai RA, Bosworth JK, Busch P, Smilgies DM, Ober CK, Russel TP, Watkins JJ (2008) Adv Mater 20:246–251
132. Yamaguchi A, Uejo F, Yoda T, Uchida T, Tanamura Y, Yamashita T, Teramae N (2004) Nat Mater 3:337–341
133. Platschek B, Koehn R, Doeblinger M, Bein T (2008) Chem Phys Chem 9:2059–2067
134. Hara M, Nagano S, Seki T (2010) J Am Chem Soc 132:13654–13656
135. Richman EK, Brezesinski T, Tolbert SH (2008) Nat Mater 7:712–717
136. Yamauchi Y, Sawada M, Komatsu M, Sugiyama A, Osaka T, Hirota N, Sakka Y, Kuroda K (2007) Chem Asian J 2:1505–1512
137. Teng Z, Zheng G, Dou Y, Li W, Mou CY, Zhang X, Asiri AM, Zhao D (2012) Angew Chem Int Ed 51:2173–2177
138. Angnes L, Richter EM, Augelli MA, Kume GH (2000) Anal Chem 72:5503–5506
139. Herzog G, Sibottier E, Etienne M, Walcarius A (2013) Faraday Discuss 164:259–273
140. Lytle JC, Stein A (2006) In: Cao G, Brinker CJ (eds) Annual reviews of nano research, vol 1. World Scientific Publishing Co. Pte. Ltd., Singapore, pp 1–79
141. Etienne M, Sallard S, Schröder M, Guillemin Y, Mascotto S, Smarsly BM, Walcarius A (2010) Chem Mater 22:3426–3432
142. Guillemin Y, Ghanbaja J, Aubert E, Etienne M, Walcarius A (2014) Chem Mater 26:1848–1858
143. Li W, Zhang M, Zhang J, Han Y (2006) Front Chem China 1:438–442
144. Leontidis E (2002) Curr Opin Colloid Interface Sci 7:81–91
145. Cox JA, Wiaderek KM, Mehdi BL, Gudorf BP, Ranganathan D, Zamponi S, Berrettoni M (2011) J Solid State Electrochem 15:2409–2417
146. Mehdi BL, Rutkowska IA, Kulesza PJ, Cox JA (2013) J Solid State Electrochem 17:1581–1590
147. Etienne M, Guillemin Y, Grosso D, Walcarius A (2013) Anal Bioanal Chem 405:1497–1512
148. Xu FF, Cui FM, Ruan ML, Zhang LL, Shi JL (2010) Langmuir 26:7535–7539
149. Etienne M, Cortot J, Walcarius A (2007) Electroanalysis 19:129–138
150. Goux A, Ghanbaja J, Walcarius A (2009) J Mater Sci 44:6601–6607
151. Etienne M, Goux A, Sibottier E, Walcarius A (2009) J Nanosci Nanotechnol 9:2398–2406
152. Guillemin Y, Etienne M, Aubert E, Walcarius A (2010) J Mater Chem 20:6799–6807
153. Vilà N, Ghanbaja J, Aubert E, Walcarius A (2014) Angew Chem Int Ed 53:2945–2950
154. Rafiee M, Karimi B, Farrokhzadeh S, Vali H (2013) Electrochim Acta 94:198–205
155. Lim MH, Stein A (1999) Chem Mater 11:3285–3295
156. Rafiee M, Karimi B, Asl YA, Vali H (2013) Analyst 138:1740–1744
157. Rafiee M, Karimi B, Arshi S, Vali H (2014) Dalton Trans 43:4901–4908
158. Herzog G, Vodolazkaya NA, Walcarius A (2013) Electroanalysis 25:2595–2603
159. Unpublished results
160. Xia S, Zhang J, Li C (2010) Anal Bioanal Chem 396:697–705
161. Maghear A, Etienne M, Tertiș M, Sandulescu R, Walcarius A (2013) Electrochim Acta 112:333–341
162. Kang HS, Lee HC, Kwak JH (2011) J Korean Electrochem Soc 14:22–26
163. del Valle MA, Gacitúa M, Díaz FR, Armijo F, del Río R (2009) Electrochem Commun 11:2117–2120
164. del Valle MA, Gacitúa M, Díaz FR, Armijo F, del Río R (2012) Electrochim Acta 71:277–282
165. Qu F, Sun H, Zhang Y, Lu H, Yang M (2012) Sens Actuat B166–167:837–841
166. Le Duc Y, Gilles A, Mihai S, Rouessac V, Tingry S, Barboiu M (2013) Chem Commun 49:3667–3669
167. Forano C, Costantino U, Prevot V, Taviot-Gueho C (2013) In *Handbook of Clay Science, Second Edition*, F Bergaya, G Lagaly (ed.), Elsevier, pp. 745-782
168. Costantino U, Leroux F, Nocchetti M, Mousty C (2013) In *Handbook of Clay Science, Second Edition Part B Techniques and Applications*, F Bergaya, G Lagaly (ed.), Elsevier, pp. 765-791
169. Dixit M, Vishnu Kamath P (1995) J Power Sources 56:97–100

170. Indira L, Kamath PV (1994) J Mater Chem 4:1487–1490
171. Guo X, Zhang F, Evans DG, Duan X (2010) Chem Commun 46: 5197–5210
172. Scavetta E, Mignani A, Prandstraller D, Tonelli D (2007) Chem Mater 19:4523–4529
173. Scavetta E, Ballarin B, Gazzano M, Tonelli D (2009) ElectrochimActa 54:1027–1033
174. Scavetta E, Ballarin B, Corticelli C, Gualandi I, Tonelli D, Prevot V, Forano C, Mousty C (2012) J Power Sources 201: 360–367
175. Yarger MS, Steinmiller EMP, Choi K-S (2008) Inorg Chem 47: 5859–5865
176. Prasad BE, Dinamani M, Vishnu Kamath P, Mehta SH (2010) J Colloid Interface Sci 348:216–218
177. Monti M, Benito P, Basile F, Fornasari G, Gazzano M, Scavetta E, Tonelli D, Vaccari A (2013) Electrochim Acta 108:596–604
178. Nejati K, Asadpour-Zeynali K (2014) Mater Sci Eng C 35:179–184
179. Obayashi C, Ishizaka M, Konishi T, Yamada H, Katakura K (2012) Electrochemistry 80:879–882
180. Brownson JRS, Lévy-Clément C (2009) Electrochim Acta 54: 6637–6644
181. Gupta V, Gupta S, Miura N (2009) J Power Sources 189:1292–1295
182. Gualandi I, Solito AG, Scavetta E, Tonelli D (2012) Electroanalysis 24:857–864
183. Scavetta E, Ballarin B, Giorgetti M, Carpani I, Cogo F, Tonelli D (2004) J New Mater Electrochem Syst 7:43–50
184. Liang H, Miao X, Gong J (2012) Electrochem Commun 20:149–152
185. Mignani A, Ballarin B, Giorgetti M, Scavetta E, Tonelli D, Boanini E, Prevot V, Mousty C, Iadecola A (2013) J Phys Chem C 117: 16221–16230
186. Yin Z, Wu J, Yang Z (2011) Biosens Bioelectron 26:1970–1974
187. Scavetta E, Ballarin B, Tonelli D (2010) Electroanalysis 22:427–432
188. Wang Y, Rui Y, Li F, Li M (2014) Electrochim Acta 117:398–404
189. Li M, Xu S, Ni F, Wang Y, Chen S, Wang L (2009) Microchim Acta 166:203–208
190. Basile F, Benito P, Fornasari G, Rosetti V, Scavetta E, Tonelli D, Vaccari A (2009) Appl Catal B 91:563–572
191. Basile F, Benito P, Fornasari G, Monti M, Scavetta E, Tonelli D, Vaccari A (2010) Catal Today 157:183–190
192. Khenifi A, Derriche Z, Forano C, Prevot V, Mousty C, Scavetta E, Ballarin B, Guadagnini L, Tonelli D (2009) Anal Chim Acta 654: 97–102
193. Prevot V, Forano C, Khenifi A, Ballarin B, Scavetta E, Mousty C (2011) Chem Commun 47:1761–1763
194. Zhao M-Q, Zhang Q, Huang J-Q, Wei F (2012) Adv Funct Mater 22:675–694
195. Kwon Y, Hong HG (2013) Bull Korean Chem Soc 34:1755–1762
196. Ju J, Bai J, Bo XJ, Guo LP (2012) Electrochim Acta 78:569–575
197. Daniel M-C, Astruc D (2003) Chem Rev 104:293–346
198. Ballarin B, Mignani A, Scavetta E, Giorgetti M, Tonelli D, Boanini E, Mousty C, Prevot V (2012) Langmuir 28:15065–15074
199. Wang Y, Ji H, Peng W, Liu L, Gao F, Li M (2012) Int J Hydrogen Energy 37:9324–9329
200. Scavetta E, Stipa S, Tonelli D (2007) Electrochem Commun 9: 2838–2842
201. Gong J, Wang L, Miao X, Zhang L (2010) Electrochem Commun 12:1658–1661
202. Parello ML, Rojas R, Giacomelli CE (2010) J Colloid Interface Sci 351:134–139
203. Prevot V, Mousty C, Forano C (2013) In *Advances in Chemistry Research* (ed.), Nova Science Publishsers,Inc, pp. 35-83
204. Mignani A, Scavetta E, Tonelli D (2006) Anal Chim Acta 577:98–106
205. Mignani A, Luciano G, Lanteri S, Leardi R, Scavetta E, Tonelli D (2007) Anal Chim Acta 599:36–40
206. Mignani A, Scavetta E, Guadagnini L, Tonelli D (2009) Sens Actuat B 136:196–202
207. Guadagnini L, Ballarin B, Mignani A, Scavetta E, Tonelli D (2007) Sens Actuat B126:492–498
208. Addari D, Mignani A, Scavetta E, Tonelli D, Rossi A (2011) Surf Interface Anal 43:816–822
209. Guadagnini L, Mignani A, Scavetta E, Tonelli D (2010) Electrochim Acta 55:1217–1220
210. Scavetta E, Guadagnini L, Mignani A, Tonelli D (2008) Electroanalysis 20:2199–2204
211. Carpani I, Guadagnini L, Tonelli D (2009) Electroanalysis 21:2401–2409
212. Mousty C, Leroux F (2012) Recent Pat Nanotechnol 6:174–192
213. Faour A, Mousty C, Prevot V, Devouard B, De Roy A, Bordet P, Elkaim E, Taviot-Gueho C (2012) J Phys Chem C 116:15646–15659
214. Li MG, Ni F, Wang YL, Xu SD, Zhang DD, Chen SH, Wang L (2009) Electroanalysis 21:1521–1526
215. Vialat P, Leroux F, Taviot-Gueho C, Villemure G, Mousty C (2013) Electrochim Acta 107:599–610
216. Basile F, Benito P, Del Gallo P, Fornasari G, Gary D, Rosetti V, Scavetta E, Tonelli D, Vaccari A (2008) ChemCommun 2917-2919
217. Ni F, Wang Y, Zhang D, Gao F, Li M (2010) Electroanalysis 22: 1130–1135
218. Carpani I, Tonelli D (2006) Electroanalysis 18:2421–2425
219. Wang YL, Zhang DD, Peng W, Liu L, Li MG (2011) Electrochim Acta 56:5754–5758
220. Ballarin B, Berrettoni M, Carpani I, Scavetta E, Tonelli D (2005) Anal Chim Acta 538:219–224
221. Gong J, Wang L, Song D, Zhu X, Zhang L (2009) Biosens Bioelectron 25:493–496
222. Scavetta E, Ballarin B, Berrettoni M, Carpani I, Giorgetti M, Tonelli D (2006) ElectrochimActa 51:2129–2134
223. Mignani A, Corticelli C, Tonelli D, Scavetta E (2011) Electroanalysis 23:1745–1751
224. Gualandi I, Scavetta E, Zappoli S, Tonelli D (2011) Biosens Bioelectron 26:3200–3206